LiDAR Remote Sensing for Vertical Distribution of Seawater Optical Properties and Chlorophyll-a From the East China Sea to the South China Sea

Peng Chen, Dong Liu, Cédric Jamet

Lidar remote sensing for vertical distribution of seawater optical properties and chlorophyll-a from the East China Sea to the South China Sea

Peng Chen*, Cédric Jamet, Dong Liu

***Abstract*—The traditional way to detect the vertical structure of seawater optical properties and chlorophyll-a is mainly through shipboard discrete observations or Biogeochemical-Argo profiling floats, which requires considerable time to cover a limited area. In this study, the vertical distribution of seawater optical properties and chlorophyll-a concentration across two different optically-contrasted sea areas from the East China Sea (ESC) to the South China Sea (SCS) were obtained for the first time using a shipboard integrated Mie-Raman-fluorescence lidar for large-scale observations, with a total observation distance of over 3700 km. More than 74,000 lidar profiles were obtained from September 5 to September 15, 2020. In general, the lidar-estimated inherent optical properties (IOPs) and chlorophyll-a values decreased from turbid water in the ECS to clear water in the SCS. Subsurface scattering layers were often observed at depths ranging from 10 to 20 m along the SCS coast. Subsequently, the lidar-derived results were compared against in situ measurements. In addition, the diurnal hourly variation in IOPs and chlorophyll-a by lidar at a fixed coastal station was monitored for the first time, which was relatively lower in the early morning and midday yet was higher in the evening, while the relative tide height showed the reverse change trend, which revealed that the tide possibly impacted the diurnal variation in IOPs and chlorophyll-a on the SCS coast. Overall, our results indicate that the lidar remote sensing technique is effective and feasible to monitor large-scale and long-term subsurface phytoplankton structure over different optically-contrasted sea regions, and integration of multiple detection mechanisms will enhance the monitoring capacity.**

***Index Terms*—lidar, subsurface phytoplankton layer, hybrid method, South China Sea, lidar attenuation coefficient, multiple scattering**

I. Introduction

Satellite passive ocean color observations can provide large-scale, frequent, and continuous views of the variability in the global ocean. It has vastly improved understanding of the distribution of phytoplankton and marine primary productivity [1]. However, these measurements are limited to clear sky, daylight, high sun elevation angles, and ice-free oceans and are exponentially weighted toward the ocean surface [2]. The traditional way to detect the vertical structure of optical properties and chlorophyll-a is often through shipboard discreate observations [3, 4] or Biogeochemical-Argo profiling floats [5], which take considerable time to cover a limited area. These limitations can be addressed by active lidar technology. Active lidar measurements could provide depth-resolved values of ocean phytoplankton properties at both day and night, over the globe and in polar regions, which are helpful to improve the estimation of global phytoplankton primary productivity and carbon stocks/fluxes [6-8] and to understand the spatiotemporal distributions of underwater plankton and their dynamic variation in the upper ocean driven by physical and biological factors [9, 10]. With new vertically resolved and diurnal continuous measurements, lidar can also provide new insights into high latitude ecosystems and diel vertical migration [8, 11]. Lidar is just such a technique and can usher in the next revolution in satellite ocean remote sensing [12].

In recent years, interest for lidar systems has been renewed and they have been proposed as an effective tool for oceanic research, as demonstrated by a variety of measurements in the upper ocean [13], including profiling optical properties [14-18], detecting bathymetry [19, 20], fish and zooplankton [21-25], subsurface phytoplankton layers [26-30], and internal waves and bubbles [31, 32]. However, there are still very few applications in Chinese seas limited to the cost and technical maturity of the instrument. In this study, the vertical distribution of seawater optical properties and chlorophyll-a concentration across two different optically-contrasted Chinese sea areas from the East China Sea to the South China Sea were obtained for the first time using a shipboard integrated Mie-Raman-

This research was funded by Key Special Project for Introduced Talents Team of Southern Marine Science and Engineering Guangdong Laboratory (Guangzhou) (GML2019ZD0602), the National Natural Science Foundation (41901305; 61991453), and the Zhejiang Natural Science Foundation (LQ19D060003). It was also supported by the Fund of the Key Laboratory of Space Active Opto-electronics Technology. (Corresponding authors: Peng Chen).

Peng Chen is with the State Key Laboratory of Satellite Ocean Environment Dynamics, Second Institute of Oceanography, Ministry of Natural Resources, 36 Bochubeilu, Hangzhou, 310012; Southern Marine Science and Engineering Guangdong Laboratory (Guangzhou), No. 1119, Haibin Rd., Nansha District, Guangzhou, China (e-mail: chenp@sio.org.cn).

Cédric Jamet is with Laboratoire d'Océanologie et de Géosciences (LOG), Université du Littoral-Côte d'Opale, Wimereux, France (cedric.jamet@univ-littoral.fr).

Dong liu is with College of Optical Science and Engineering, Zhejiang University, Hangzhou, 310027, China (e-mail: liudongopt@zju.edu.cn).

fluorescence lidar. More than 74,000 lidar profiles were observed from September 5 to September 15, 2020. The signals of parallel and perpendicular polarized Mie scattering, Raman scattering, and fluorescence were obtained simultaneously. Spatial and diurnal variation in the vertical distribution of optical properties and chlorophyll-a retrieved by the lidar data were analyzed.

This article is organized as follows. In Section 2, an integrated Mie-Raman-fluorescence lidar system, the study area and a hybrid retrieval method used in this research are introduced. The horizontal and vertical distributions of inherent optical properties (IOP) and chlorophyll-a retrieved by the lidar data along the vessel tracks, diurnal variation of IOPs and chlorophyll-a at a fixed station, and comparisons between lidar-derived and in situ-observed data are presented in Section 3. Finally, the summary and conclusion are provided in Section 4.

II. Materials and Methods

A. *Integrated Mie-Raman-fluorescence lidar system*

An integrated Mie-Raman-fluorescence lidar (MRFL) was developed by the College of Optical Science and Engineering, Zhejiang University. The transmitting part is mainly composed of a Nd:YAG pulse laser with a green band. After a series of collimating beam expanding systems, laser pulses with narrow pulse widths are emitted into the ocean. A 532 nm pulsed laser was utilized with a pulse energy of 5 mJ, repetition rate of 10 Hz, and pulse width of 8 ns. The receiving part consists of a telescope, a field-of-view aperture, a collimating lens, an interference filter, a receiving lens and a photodetector. A telescope with a diameter of 80 mm and a field of view of 200 mrad was employed. The bandwidth of the interference filter we use in the lidar system is 3 nm. Considering the relationship between the maximum receiving field of view and the center wavelength, the center wavelength of the selected filters moves appropriately to the short wavelength. According to the geometrical relationship between the telescope and the laser, the overlap factor can be calculated. The overlap factor of the MRFL usually reaches 1 after a distance of two meters. Therefore, when studying the signal of seawater, the influence of the overlap factor on the echo signal can be ignored under the condition that the incident optical axis and the receiving optical axis are parallel. The field of view aperture is placed on the focal plane of the telescope, and the receiving field of view angle can be adjusted by adjusting the aperture. An interference filter is placed behind a collimating lens to filter out background light. The photodetector is located behind the convergent lens and is used to convert optical signals into electrical signals. There are four PMT detectors for receiving signals of parallel polarization Mie scattering, perpendicular polarization Mie scattering, Raman scattering and fluorescence. The detector efficiency is larger than 18%. In addition, the analog digital converter (ADC) has a bandwidth of 200 MHz, with a sample rate of 400 MS/s, which corresponds to a vertical resolution of approximately 0.282 m in water. The resolution of the ADC is 14 bits with four acquisition channels. The total weight of the system is 60 kg, and the bulk volume is 0.2 m^3. Figure 1 shows the schematic diagram, and Table 1 shows the detailed parameters for the MRFL system. Figure 2 shows photos of the lidar system taken at day and night.

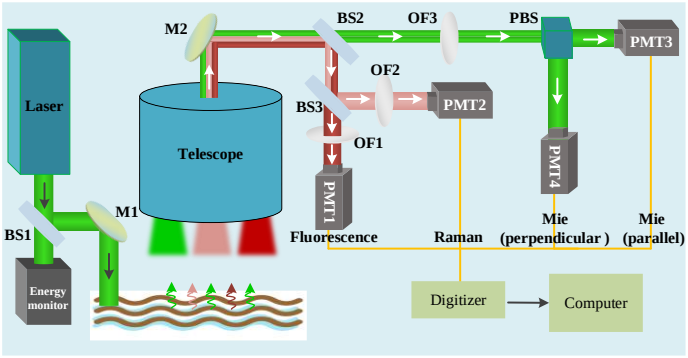

Fig. 1. Schematic diagram of the MRFL system. BS1, BS2, BS3: beam splitter; M1, M2: mirror; PBS: polarizing beam splitter; OF1, OF2, OF3: optical filter; PMT1, PMT2, PMT3, PMT4: photomultiplier tubes.

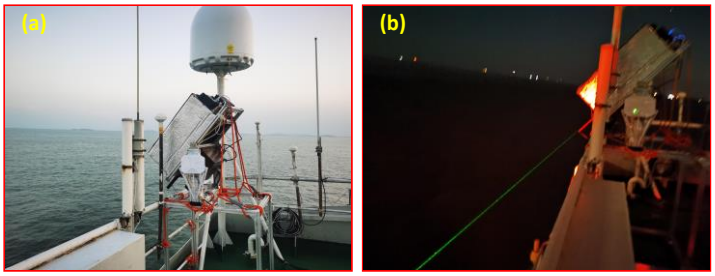

Fig. 2. Photos of the MRFL system taken at day (a) and at night (b).

TABLE I
DETAILED PARAMETERS DESIGNED FOR THE MRFL SYSTEM

Laser	
Wavelength	532 nm
Pulse energy	5 mJ
Repetition rate of laser	10 Hz
Pulse width	8 ns
Polarization state	Horizontal
Beam Divergence	<1 mrad
Beam diameter	8 mm
Receiver	
Diameter of telescope	80 mm
Field of view	200 mrad
Interference filter bandwidth	3 nm @532 nm; 10 nm @ 650, 685 nm
Interference filter efficiency	>70%
Detector Efficiency	> 18%
Anode responsivity	0.3 A/W
Detector	PMT
Analog Digital Converter	
Bandwidth	200 MHz
Sample rates	400 MS/s
Resolution	14 bit
Channels	4

	Others
Weight	60 kg
Bulk volume	0.2 m^3
Device control interface	Standard network interface
Software platform	Windows 10

B. Study area

The MRFL lidar system was deployed aboard the 'Runjiang' scientific expedition vessel, allowing continuous sampling from Zhoushan, East China Sea (ECS) to Sanya Bay, South China Sea (SCS) (Figure 3). The lidar measurement tracks covered both the turbid water in the ECS and the clear water in the SCS, with a total traveling distance over 3700 km. The whole investigation voyage lasted nearly two weeks from September 5 to September 15, 2020. Among them, the lidar made continuous measurements throughout the whole day at a fixed station (110.4434°E, 18.6024°N) on September 14. During the investigations, the lidar was mounted on the vehicle deck approximately 18 m above the sea surface at an angle of approximately 40° from nadir. Figure 3 shows the map of shipborne lidar measurement tracks and synchronous discrete in situ validation stations from the ECS to the SCS. The colored lines are lidar-observed tracks, and red triangles are in situ traditional optical measurement stations. The contour map represents the bathymetry variation and shows that the lidar-observed tracks are below a depth of 50 m in the ECS and mostly above a depth of 50 m in the SCS.

Simultaneously, in situ validation for lidar measurements was conducted by traditional commercial bio-optical instruments. A total of 63 in situ survey stations were designed along the lidar measurement tracks. Among them, the Stations from S50 to S62 are at a fixed station measured every 2 hours for a whole day. At each station, inherent optical properties (IOPs) were measured over depths ranging from 0 to 60 m using an absorption and attenuation meter (AC-S, Wetlab Ltd., America) and a backscatter meter (Hydroscat-6, HOBILabs Ltd., America). Chlorophyll-a fluorescence was measured using a multiparameter water quality monitor (RBR XR-420, RBR Ltd., Canada), and the fluorescence data were calibrated to extract chlorophyll-a concentration using a laboratory scanning spectrofluorometer (Trilogy, Turner Designs Inc.) [33]. The diffuse attenuation coefficient K_d was calculated by absorption and backscattering coefficients based on the Lee's model [34]. Among them, the AC-S operated successfully after Station S7, and the RBR failed to run after Station S48. Detailed in situ data information is presented in Table A1 in Appendix A.

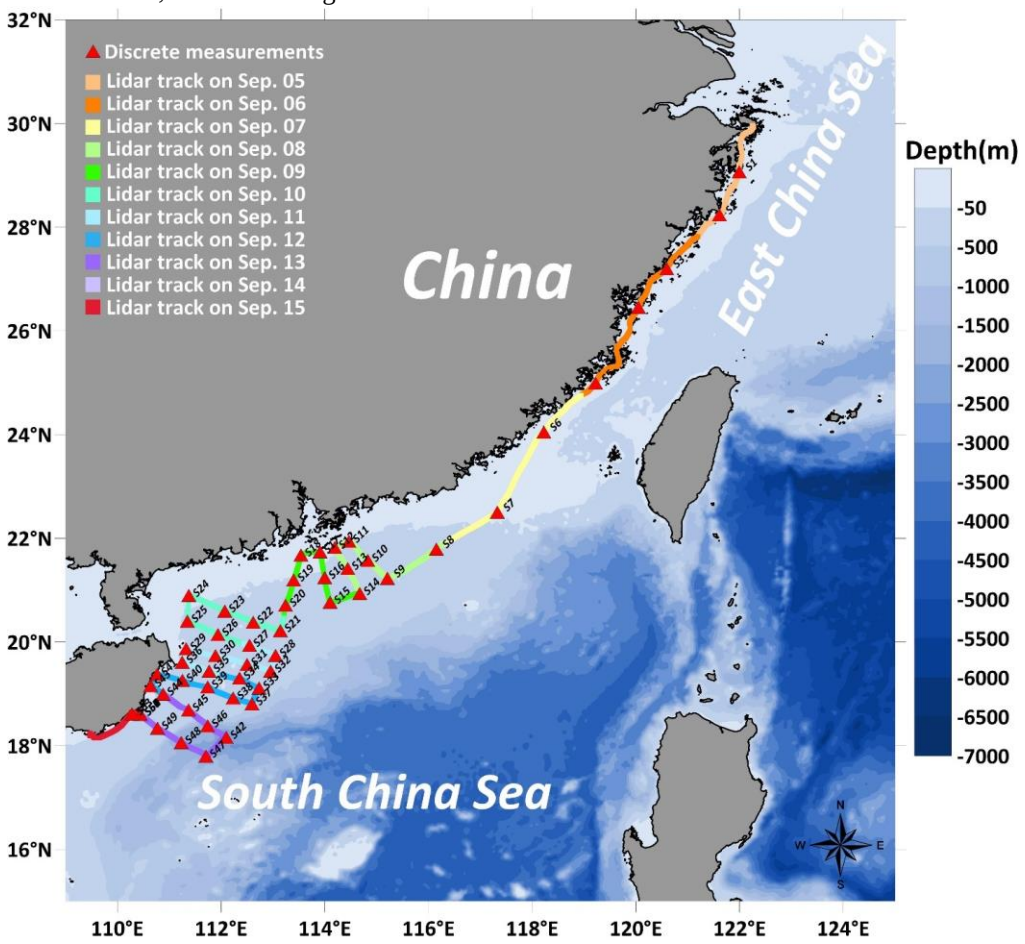

Fig. 3. Map of shipborne lidar measurement tracks and synchronous discrete in situ validation stations from ECS to SCS from September 05 to September 15, 2020. The colored lines are lidar-observed tracks, and red triangles are in situ traditional optical measurement stations. The contour map represents the bathymetry

variation and shows that the lidar-observed tracks are below a depth of 50 m in the ECS and mostly above a depth of 50 m in the SCS. The bathymetry data is from the ETOPO1 Global Relief Model by the National Geophysical Data Center (NGDC) [35].

C. Lidar hybrid retrieval model

A hybrid retrieval method [15, 26] was proposed to estimate the lidar extinction coefficient k_{lidar} and the backscatter coefficient at 180 degrees $\beta_\pi(z)$ based on the integration of the Klett retrieval method [36] and the perturbation retrieval (PR) method [17]. The lidar measured signal was calibrated by an iterative method [33].The Klett method assumes that there is a relationship between $k_{\text{lidar}}(z)$ and $\beta_\pi(z)$, and the PR method assumes that the water optical parameters can be expressed as the sum of a part that does not vary with depth $S_h(z)$ and a varying part. Then, the $k_{\text{lidar}}(z)$, $\beta_\pi(z)$, and b_{bbp} could be estimated:

$$k_{lidar}(z) = \frac{\exp\left[\frac{S(z)-S_m}{r}\right]}{\left\{\frac{1}{k_{lidar}(m)}+\frac{2}{r}\int_z^{z_m}\exp\left[\frac{S(z)-S_m}{r}\right]d_z\right\}} \quad (1)$$

$$\beta_\pi(z) = \frac{S(z)}{S_h(z)}\beta_\pi(0) \quad (2)$$

$$S(z) = ln(P(z)\times z^2)) \quad (3)$$

$$S_h(z) = ln(A\beta_\pi^{non}) - 2k_{lidar}^{non} \quad (4)$$

$$k_{lidar}(m) = -\frac{1}{2}\frac{dS_m}{dZ_m} \quad (5)$$

$$b_{bp} = 2\pi\chi(\theta)\beta(\theta) \quad (6)$$

$$\beta_\pi(0) = \frac{exp(S(0))}{A} \quad (7)$$

where $P(z)$ is the instantaneous received power at depth z, $S(z)$ is the logarithmically transformed range-corrected power of $P(z)$, r is an exponential parameter that depends on the wavelength and water optical characteristics, which is often equal to 1, m is the reference depth, S_m is the lidar power at the reference depth and $k_{lidar}(m)$ is the lidar attenuation coefficient at the reference depth, which can be obtained using the slope method, in which the reference depth is often the depth where the lidar signal intensity is one percent of the maximum signal intensity. It was found the $k_{lidar}(m)$ has a relatively small effect on the accuracy of the retrieved k_{lidar} with increasing range between z and z_m [14]. A is the lidar system constant accounting for an integrated function of laser energy, the optical efficiency of the receiver, the detector electronic gain and, among others [33], $\beta_\pi(0)$ and S(0) are the backscatter coefficient and $S(z)$ at the sea surface, and k_{lidar}^{non} and β_π^{non} are the mean nonvarying parts for k_{lidar} and β_π, which could be obtained from the linear fitting calculation of $S_h(z)$ for $S(z)$. Because lidar has a large field of view, k_{lidar} approaches the water diffuse attenuation coefficient k_d in this study [37-40]. The relationship between b_{bbp} and $\beta(\theta)$ can be expressed by Equation (6), where $\beta(\theta)$ is the volume scattering function (VSF) at θ and $\chi(\theta)$ is a conversion factor. There is an uncertainty for this model in $\chi(180°)$. Most VSF instruments could only measure the VSF at angles up to 170° due to that the measurements at angles $> 173°$ are unreliable due to stray light contamination [41-45]. Some studies reports the estimated $\chi(180°)$ was approximately 1.43 [46, 47], some report it was 1.06 [18, 30, 48], while others report it was 0.5 [49-51]. In this study, we measured both b_{bbp} and $\beta(140°)$ using the Hydroscat-6 instrument [52]. The scatter plot of the regression analysis result is shown in Figure A1 in Appendix A, and the calculated $\chi(140°)$ was 1.08 and the estimated $\chi(180°)$ was approximately 1.08 based on the Sullivan's measurements [53, 54] that the χ factor has been assumed to be 1.076 at all wavelengths.

There may be a range ambiguity problem which could mix up the light signals scattered from various depth, which means the weaker signal from deeper water could be contaminated by the decay signal from the upper water. It also named "pulse stretching" by some previous studies [55-58]. The idea of a system without time dispersion is a mathematical convenience. It is never absolutely correct. Any photon deflected from the beam axis encounters a time delay in reaching the target plane. The time excess is the multipath time, τ=t-z/c. When the multipath time is small compared with other system time constraints, such as the laser pulse length, the dispersion-less system concept is justifiable. A theoretical basis is provided for the time-dependent lidar equations in the forward-scattering regime based on the beam spread function with time dispersion as a Green's function [57]. The Monte Carlo numerical method is an alternative to the analytical approach and inherently includes pulse stretching along with beam spreading. Based on previous studies, if the receiver FOV is sufficiently large, the complex analytical approximation reduces to a commonly used lidar equation and the derived k_{lidar} approaches to k_{d}. In addition, there may be an issue that a slow transient recovery occurs for some PMTs, in which the signal arising from a strong surface return is spread over several adjacent range bins starting from the bin that contains the surface echo [13, 59]. In this study, the lidar has a large incident angle (40-degree off nadir angle) and fast transient recovery of the PMTs, which is hard to receive the specular reflection of strong backscattering signal at the backward direction, and a return spreading over several adjacent range bins by the PMTs could not occur.

III. Results and Discussion

A. An example of lidar echo signals

Figure 4 shows an example of the lidar echo signals for the MRFL. The colored lines are the signals of parallel Mie scattering, perpendicular Mie scattering, Raman scattering at 650 nm and chlorophyll fluorescence at 685 nm. The various lidar signals are in a.u., and they are digitized signals with the relative magnitudes between them accurate. The signals gradually decrease due to sea water attenuation, while the signal decay rates are different for the four signal channels. The fluorescence and Raman signals (685 nm and 650 nm) have a larger decay rate than the Mie scattering signal (532 nm). Therefore, it appears that the maximum detection depth for fluorescence and Raman signals were no more than 12 m, compared to the maximum detection depth of nearly 40 m for Mie scattering signals. The parallel Mie scattering signal appears to have a little larger decay rate than the perpendicular Mie scattering signal due to the depolarization impacted by multiple scattering [60]. It can be seen that both the parallel polarization and perpendicular polarization Mie scattering

signals started to increase at approximately 25 m. This revealed that there may be a subsurface scattering layer starting from a depth of approximately 25 m. The depolarization should be helpful for detecting the subsurface scattering layer.

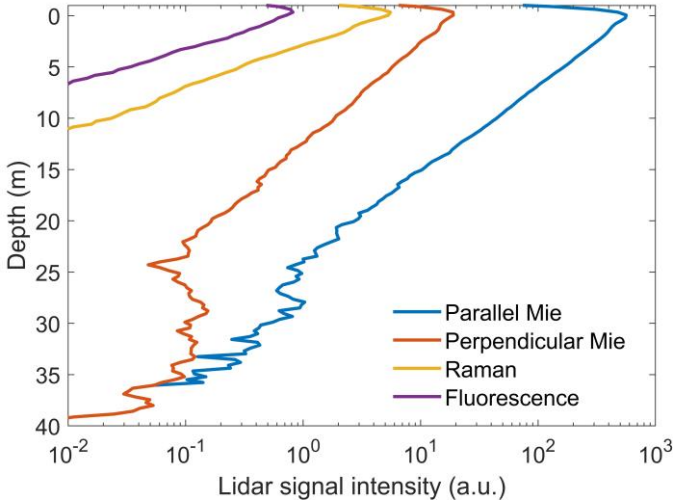

Fig. 4. An example of the lidar echo signals for the MRFL. The colored lines are the signals of polarized Mie scattering, Raman, and fluorescence.

B. Lidar signal profiles along the vessel tracks

Figure 5 shows the lidar echo signals of polarized Mie scattering as a function of depth along the vessel traveling tracks. The signals range from the sea surface to the depth of 40 m below the sea surface. The left panels ranging from top to bottom (Figs. 5(1), 5(3), …5(21)) correspond to the lidar echo signals of parallel polarization Mie scattering obtained from September 5 to September 15, 2020. The right panels ranging from top to bottom (Figs. 5(2), 5(4), …5(22)) correspond to the lidar echo signals of perpendicular polarization Mie scattering obtained from September 5 to September 15, 2020. The vertical profiles of lidar signals vary as the observation positions varied along the tracks, which reveals the variation in seawater optical properties as the vessel travels from the ECS to the SCS. The intensities of the lidar signal vertical profile measured on September 5 appear very strong, as shown in Figure. 5(1) was due to the estuarine outflow from the Yangtze River and Hangzhou Bay making these seawaters very turbid. Although it appears that there are still lidar echo signals at depths below 15 m, as shown in panels 5(1) to 5(4), in fact, the lidar maximum penetration depth in these turbid regions is basically no more than 15 m, the echo signals at depths below 15 m were mainly noise signals due to low signal to noise ratio after the depth, because the signal intensity decreases rapidly in turbid water [11]. It can be seen that the lidar maximum penetration depths begin to increase considerably in Figure. 5(5) (the blue color regions begin to appear), which was because the water became clear when the vessel reached the coast of Fujian Province. The maximum lidar penetration depth increased from 15 m to 40 m as the vessel traveled from the ECS to the SCS. This revealed that lidar could rapidly monitor the spatial variations in seawater turbidity or seawater transparency at a large scale based on lidar echo intensity variations. It also showed that the sea floors or subsurface plankton in some areas off the SCS coast may be detected, such as those in Figures. 5(16), 5(21) and 5(22).

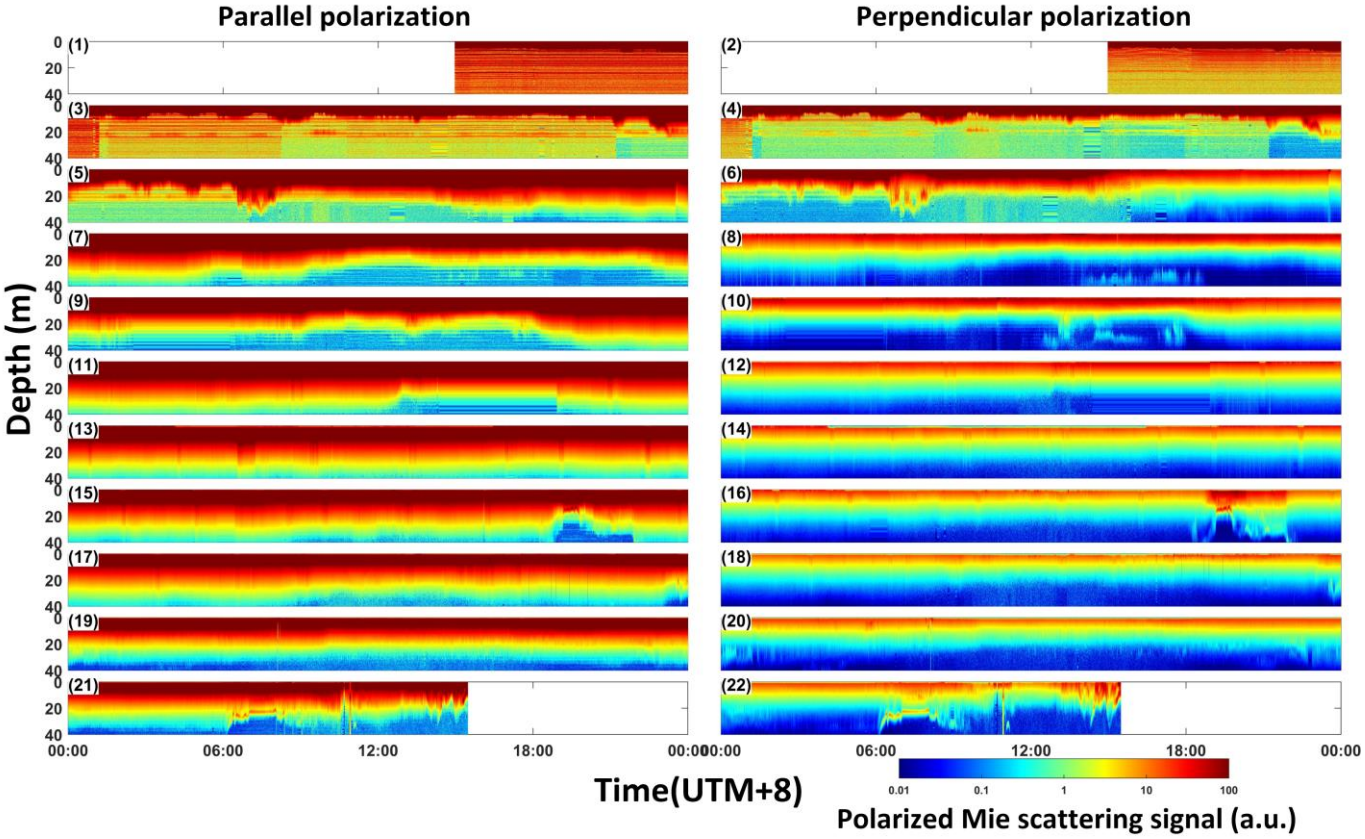

Fig. 5. Map of lidar echo signals of polarized Mie scattering along the ship traveling tracks. The left panels ranging from Fig. 5(1) to Fig. 5(21) correspond to the lidar echo signals of parallel polarization Mie scattering obtained from September 5 to September 15, 2020, respectively. The right panels ranging from Fig. 5(2) to Fig. 5(22) correspond to the lidar echo signals of perpendicular polarization Mie scattering obtained from September 5 to September 15, 2020, respectively.

Figure 6 shows the lidar echo signals of fluorescence and Raman scattering along the vessel traveling tracks. The signals range from the sea surface to the depth of 8 m below the sea surface. The left panels ranging from top to bottom (Figs. 6(1), 6(3), …6(21)) correspond to the lidar echo signals of fluorescence at 685 nm obtained from September 5 to September 15, 2020. The right panels ranging from top to bottom (Figs. 6(2), 6(4), …6(22)) correspond to the lidar echo signals of Raman scattering at 650 nm obtained from September 5 to September 15, 2020. The vertical profiles of lidar signals vary as the observation position varied along the tracks, which reveals the variation in chlorophyll-a concentration as the vessel traveled from the ECS to the SCS. Strong signals are observed just under the surface (up to 2 meters) in panels 6(1) to 6(10) which could be related to the presence of phytoplankton. The fluorescence signal then decreases and is very low for panels 6(11) to 6(21), in the open ocean waters. The Raman signal also decreases for these areas but remains quite strong. It also appears that the signals during the daytime are noisy compared to those during the nighttime due to the influence from solar background light.

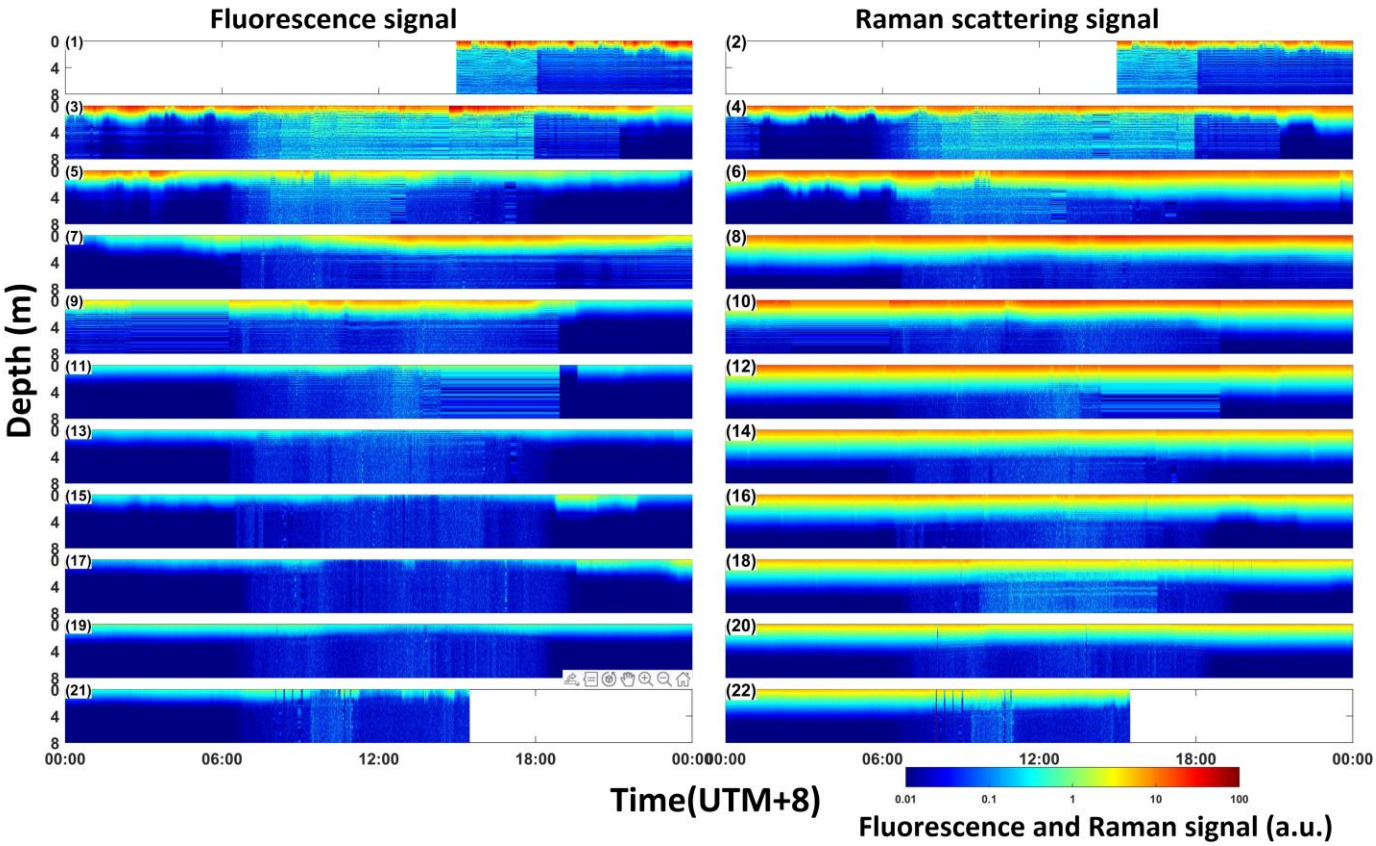

Fig. 6. Map of lidar echo signals of fluorescence and Raman scattering along the ship traveling tracks. The left panels ranging from Fig. 6(1) to Fig. 6(11) correspond to the lidar echo signals of fluorescence obtained from September 5 to September 15, 2020, respectively. The right panels ranging from Fig. 6(2) to Fig. 6(22) correspond to the lidar echo signals of Raman scattering obtained from September 5 to September 15, 2020, respectively.

Figure 7 shows the lidar echo signals of depolarization (the ratio of perpendicular signal divided by parallel signal) along the vessel traveling tracks. The signals ranged from the sea surface to the depth of 40 m below the sea surface. The panels ranging from top to down (Figs. 7(1), 7(2), …7(11)) correspond to the lidar echo signals of depolarization obtained from September 5 to September 15, 2020. The vertical profiles of lidar depolarization signals vary as the observation position varied along the tracks, which reveals the variation in optically-active particles as the vessel traveled from the ECS to the SCS. This is especially true for the coastal areas (panels 7(1) to 7(3)). This also shows that the sea floors in some areas off the ESC coast and SCS coast were detected, such as those in Figures. 7(8) and 7(11). Compared to the detection results of sea floors in Figure 4, the sea floor detected by lidar depolarization signals was more pronounced and visible. The polarization signal is helpful to enhance the ability for underwater target monitoring [61, 62].

This article has been accepted for publication in IEEE Transactions on Geoscience and Remote Sensing. This is the author's version which has not been fully edited and content may change prior to final publication. Citation information: DOI 10.1109/TGRS.2022.3174230

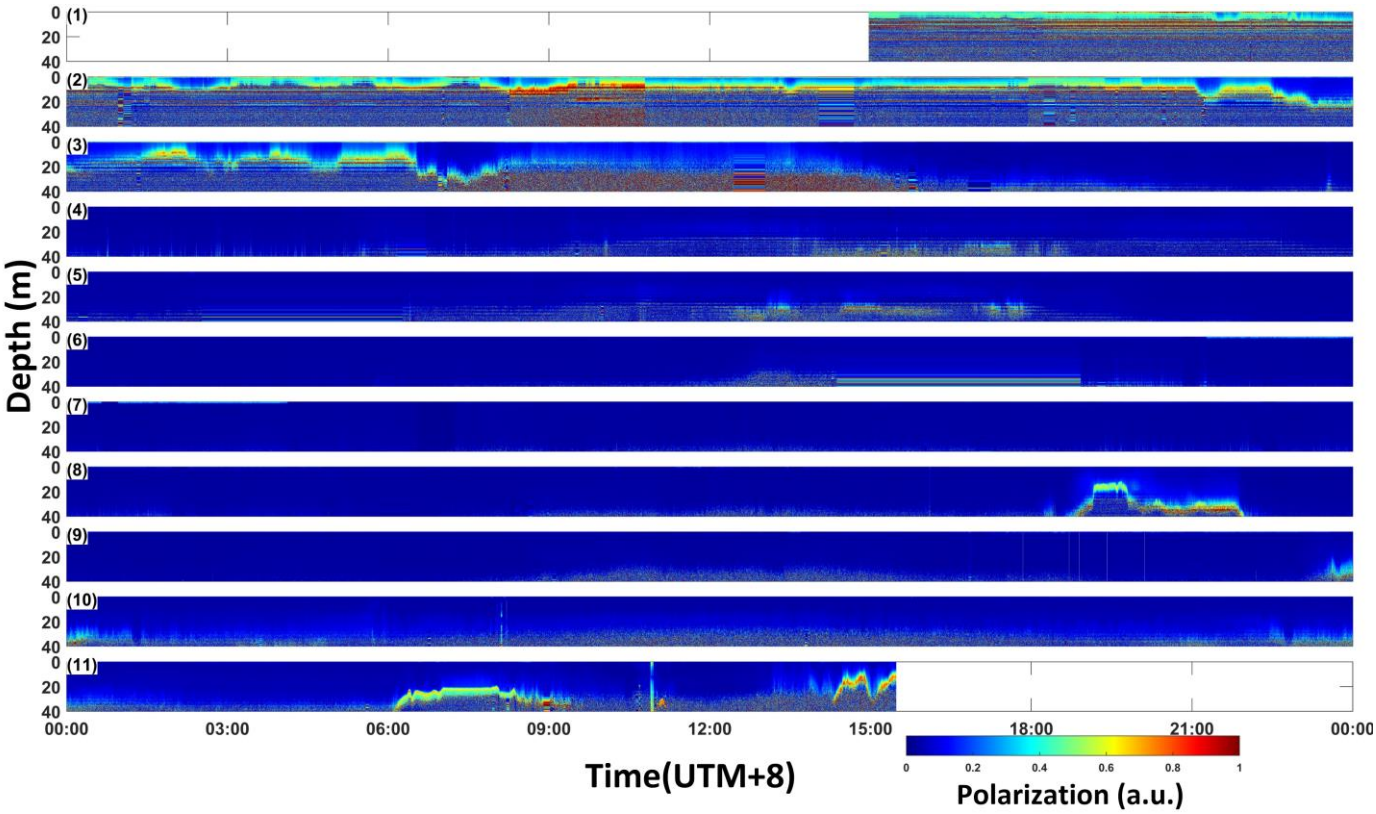

Fig. 7. Map of lidar echo signals of depolarization along the ship traveling tracks. The panels ranging from Fig. 7(1) to Fig. 7(11) correspond to the lidar echo signals of depolarization from September 5 to September 15, 2020, respectively.

Figure 8 shows the lidar echo signals of Raman normalized fluorescence (the ratio of fluorescence signal divided by Raman scattering signal) along the vessel traveling tracks. These two receiver channels of fluorescence and Raman signals were calibrated by the Luo's method [63]. Here, a water Raman signal was used for normalization of the laser fluorescence to correct the effects accounting for water environmental variation and lidar observation geometry [64, 65]. The signals ranged from the sea surface to the depth of 8 m below the sea surface. The panels ranging from top to bottom (Figs. 8(1), 8(2), …8(11)) correspond to the lidar Raman normalized fluorescence obtained from September 5 to September 15, 2020. The echo signals in panels 8(1) to 8(3) are noisy just like those in Figure 7. The vertical profiles of lidar Raman normalized fluorescence signals varied as the observation position varied along the tracks, which reveals the variation in chlorophyll-a concentration as the vessel traveled from the ECS to the SCS. The Raman normalized fluorescence signals appear larger in the ECS than in the SCS.

This article has been accepted for publication in IEEE Transactions on Geoscience and Remote Sensing. This is the author's version which has not been fully edited and content may change prior to final publication. Citation information: DOI 10.1109/TGRS.2022.3174230

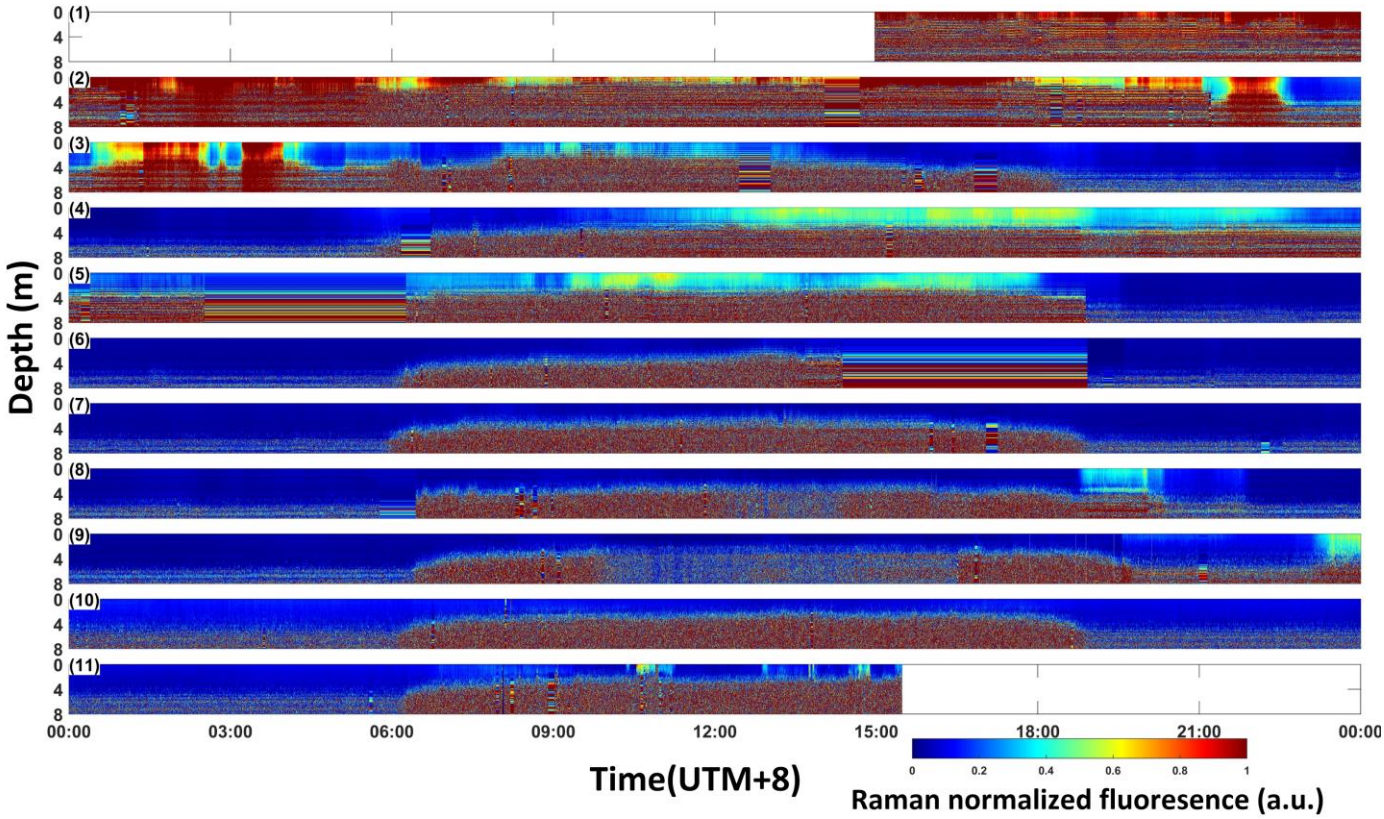

Fig. 8. Map of lidar echo signals of Raman normalized fluorescence along the ship traveling tracks. The panels ranging from Fig. 8(1) to Fig. 8(11) correspond to the lidar Raman normalized fluorescence from September 5 to September 15, 2020, respectively.

C. Horizontal distributions of IOPs and chlorophyll-a

Figure 9 shows the horizontal distributions of optical properties and chlorophyll-a in seawater along the vessel traveling tracks from the ECS to the SCS. These data were obtained by traditional bio-optical instruments. Figure 9(a) presents the horizontal distributions of chlorophyll-a, Figure 9(b) displays the horizontal distributions of the particle absorption coefficient $a_p(532)$, Figure 9(c) shows the horizontal distributions of the particle attenuation coefficient $c_p(532)$, and Figure 9(d) shows the horizontal distributions of particle backscattering b_{bp} at 550 nm. There are no $b_{bp}(532)$ because Hydroscat-6 could measure the backscattering coefficients at 442, 488, 550, 620, 700, and 852 nm [52]. There are no a_p and c_p measurements in the nearshore regions of the ECS because the absorption and attenuation meter did not operate successfully in this region in very turbid water (Figs. 9(b) and 9(c)). It can be seen that chlorophyll-a, a_p, c_p, and b_{bp} appeared to have similar horizontal distributions. Chlorophyll-a, a_p, c_p, and b_{bp} appear larger on the ECS coast, the SCS coast, and the Pearl River estuary (large green circles) than in the open sea of the SCS (small orange circles). Chlorophyll-a ranged from approximately 0.01 to 0.3 μg/L in the open sea of the SCS, ranging from 0.3 to 3 μg/L on the SCS coast, and ranging from 3 to 8 μg/L on the ECS coast and Pearl River estuary. a_p ranged from approximately 0.04 to 0.046 m^{-1} in the open sea of the SCS, ranging from 0.046 to 0.05 m^{-1} on the SCS coast, and ranging from 0.05 to 0.09 m^{-1} in the Pearl River estuary. c_p ranged from approximately 0.05 to 0.1 m^{-1} in the open sea of the SCS, ranging from 0.1 to 0.2 m^{-1} on the SCS coast, and ranging from 0.2 to 0.5 m^{-1} in the Pearl River estuary. b_{bp} ranged from approximately 0.001 to 0.002 m^{-1} in the open sea of the SCS, ranging from 0.002 to 0.003 m^{-1} in the SCS coast, and ranging from 0.003 to 0.35 m^{-1} in the Pearl River estuary and ECS coast. The relationship between chlorophyll-a concentration and b_{bp}, and chlorophyll-a concentration and a_p were compared. As shown in Figure 10, there was a relatively good agreement between chlorophyll-a and IOPs, which reveals the potential of quantifying phytoplankton using lidar-derived IOPs. There are different regression models for the data in the SCS and those in the ESC, respectively. It has a relationship of $y = 0.0088 \times x^{1.59}$ for the SCS data, with the determination coefficient (R^2) of 0.68, root mean squared error (RMSE) of 0.0027 m^{-1}, and relative error of 45.5%; while it has a relationship of $y = 0.000029 \times x^{4.38}$ for the ESC data, with the R^2 of 0.78, RMSE of 0.044 m^{-1}, and relative error of 48.6%. It also shows a higher R^2 for chlorophyll-a vs. b_{bp} compared with the relationship for chlorophyll-a vs. a_p, and the relationship between chlorophyll-a and a_p is not great. b_{bp} and particulate scattering b_p has a ratio relationship $\frac{b_{bp}}{b_p} = 0.002 + 0.01[0.5 - 0.25\log_{10}(chl)]$ [44, 53, 66]. There are different models relating chlorophyll and b_p in the past. Some studies reported the model $b_p(550) = 0.416C^{0.766}$ [67], where C represents the total chlorophyll concentration, some reported a more complex model $b_p(\lambda) = \sum_{i=1}^{3} b_p^*(\lambda)\, C_i$, where b_p^*

represents the chlorophyll specific particle backscattering coefficient and i represent pico-, nano- and micro phytoplankton, respectively [54, 68, 69], while others reported it was $b_p(660) = 0.252C^{0.635}$ [70, 71]. In this study, the model parameters were different due to that the measurements were across two different optically-contrasted Chinese sea areas, from very turbid seawater in the ECS to clear seawater in the SCS. The high exponent between b_{bp} and chlorophyll-a concentration maybe due to the impact from high concentration suspended sediment in the ECS.

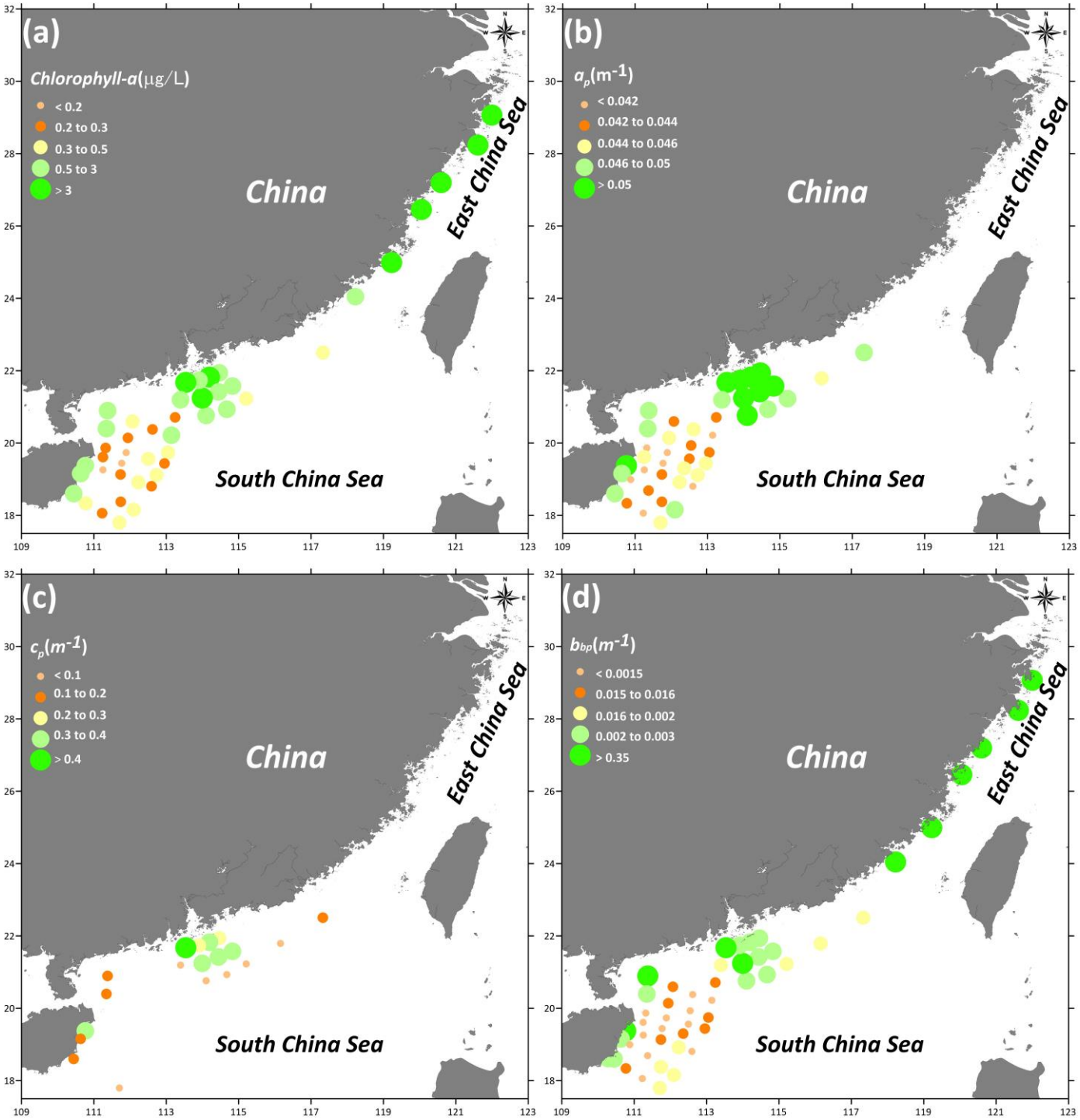

Fig. 9. Horizontal distributions of IOPs and chlorophyll-a in seawater along the vessel traveling tracks from the ECS to the SCS. (a) Horizontal distributions of chlorophyll-a; (b) horizontal distributions of the particle absorption coefficient; (c) horizontal distributions of the particle attenuation coefficient; (d) horizontal distributions of particle backscattering.

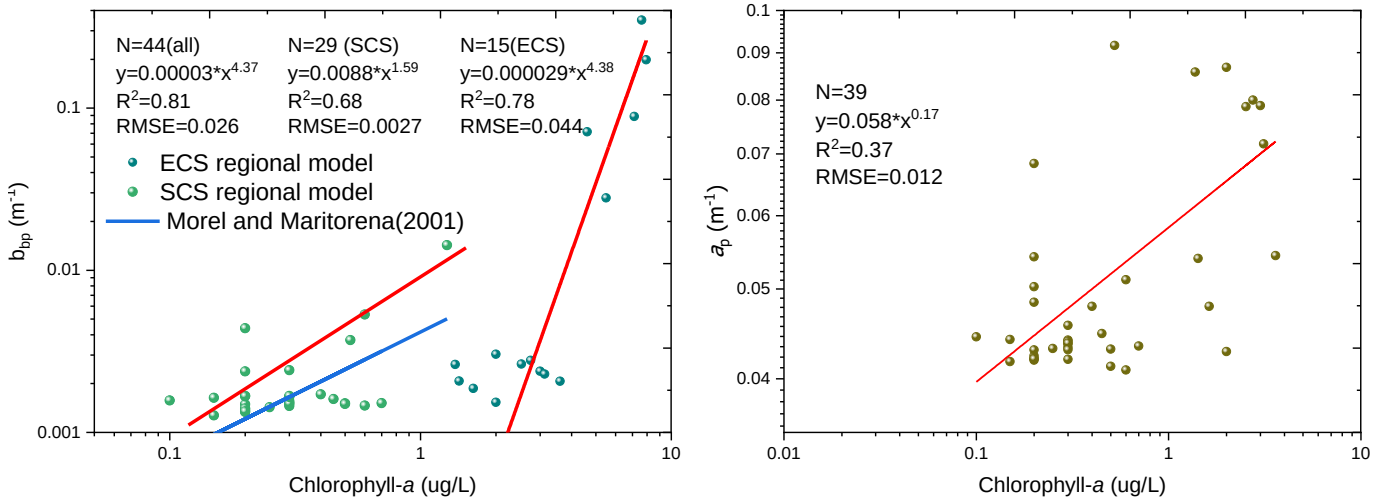

Fig. 10. The relationship between in situ-measured chlorophyll-a and IOPs. (a) chlorophyll-a vs. b_{bp}; (b) chlorophyll-a vs. a_p.

D. Vertical distributions of IOPs and chlorophyll-a

Figures 11, 12, 13 and 14 show the vertical distributions of IOPs (K_{lidar}, β(π), and b_{bp}) and chlorophyll-a concentration derived by lidar associating with GPS position information. Among them, the K_{lidar} was obtained by Eq. (1) in this study, β(π) was calculated by Eqs. (2-5), b_{bp} was obtained by Eq. (6), and chlorophyll-a concentration was derived from the regression relationship between b_{bp} and chlorophyll-a concentration in Figure 10(a). Figure 11 shows the vertical distributions of the lidar attenuation coefficient in seawater along the vessel traveling tracks from the ECS to the SCS. The panels ranging from Figures 11(a) to 11(k) correspond to the lidar-estimated K_{lidar} from September 5 to September 15, 2020. The range values of the color bars for Figures 11(a) and 11(b) are [0.05 m^{-1}: 0.5 m^{-1}] when the observations were in turbid water, while it is [0.05 m^{-1}: 0.2 m^{-1}] for the color bars from Figures 11(c) to 11(j) when the observations were in clear water. As shown in Figure 11, the estimated values varied obviously from the ECS coast to the Pearl River Estuary to the offshore and open sea of the SCS. In Figure 11(a), there was a continuous, strong subsurface maximum layer at depths from 2 to 5 m. The maximum signal occurred at approximately 2 m, and as the latitude and longitude decreased in the sea area from Zhejiang Province toward Fujian Province, the maximum depth of the signal value gradually dropped to 5 m. Figure 11(b) shows that the subsurface water attenuation coefficient below a depth of 6 m was smaller than the surface value. There was a subsurface maximum layer at depths from 6 to 10 m after the position (24.98°N, 119.22°E). In Figure 11(c), as the vessels traveled into the sea area in Guangzhou Province, the water clarity gradually varied from turbid to clear, the estimated value became weaker and discontinuous, and the maximum value depth increased. A strong subsurface maximum layer signal appeared and fell from 5 m to 20 m from the position (23.57°N, 117.91°E) to the position (22.74°N, 117.47°E) along the observation track. Figures 11(d) and 11(e) show the vertical distribution in the Pearl River Estuary. When the vessel reached the Pearl River Estuary, there was a sudden increase in the subsurface signal value, while when it left away from the coast, a sudden decrease in the subsurface signal value was observed. Additionally, the maximum depth of the subsurface layer signal seemed to rise from 25 m to 10 m at the position (21.2°N, 114° E), as shown in Figure 11(e). Actually, when subsurface layers at 5-20m were observed, lidar could hardly get any signal from the depth below 20m mainly due to the strong attenuation. It doesn't mean there was no layer below 20m. It should be noted that although the "observed" maximum depth of the layer rose from 25m to 10m, it's not certain that the "real" maximum depth of the layer rose or not. Figures 11(f) to 11(i) show the vertical distribution in the eastern South China Sea. As the water body became very clear, there was no obvious subsurface maximum layer within the depth of 25 m. In Figures 11(f) and 11(h), the vessel reached the SCS coast, a strong signal occurred from the position (20.82°N 111.57°E) to the position (20.21°N 111.78°E) and from the position (19.37°N 110.83°E) to the position (19.15°N 111.66°E) along the observation track. Figures 11(j) and 11(k) show the vertical distribution on the southern SCS coast, and the signal value increased as the vessel traveled from open sea water to coastal water. The subsurface maximum layer appeared at depths from 5 m to 15 m. Figures 12 to 14 show the vertical distributions of β(π), b_{bp} and chlorophyll-a concentration derived by lidar along the vessel traveling tracks, respectively, and they appeared to have a similar spatial variation pattern. The reason is that both the factors to calculate lidar b_{bp} from lidar β(π) and to calculate lidar chlorophyll-a concentration from lidar b_{bp} are constant. Accordingly, those three parameters derived from lidar definitely have exactly same trend. As shown in Figs. 11(d), 12(d), 13(d) and 14(d), the layer depth and thickness of subsurface chlorophyll, K_{lidar}, β(π), and b_{bp} appeared a slight difference from each other, which may be due to the model uncertainty. Similar results were observed in Figs. 11(e), 12(e), 13(e) and 14(e), and in Figs. 11(j-k), 12(j-k), 13(j-k) and 14(j-k). As shown in Figs. 11(a), 12(a), 13(a) and14(a), the thickness of subsurface scattering maximum layers was different from that of chlorophyll-a, which was due to that the IOPs were influenced combinedly by organic and inorganic particles in

seawater in the ECS.

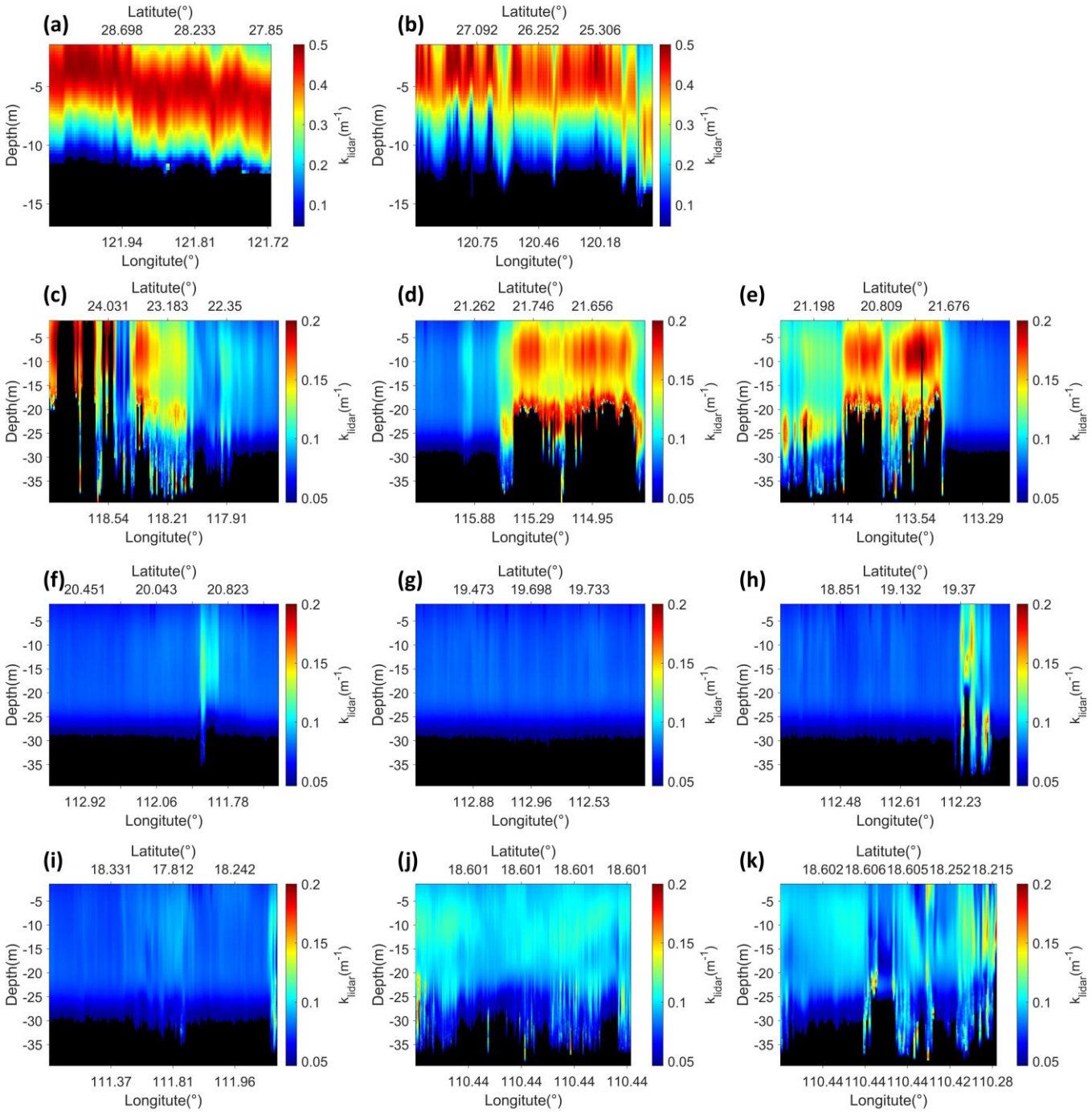

Fig. 11. Vertical distributions of the lidar-derived K_{lidar} in seawater along the vessel traveling tracks from the ECS to the SCS. The panels ranging from (a) to (k) correspond to the lidar-estimated results from September 5 to September 15, 2020, respectively. The range values of the color bars for (a) and (b) are [0.05 m^{-1}: 0.5 m^{-1}], while it is [0.05 m^{-1}: 0.2 m^{-1}] for the color bars from (c) to (j).

This article has been accepted for publication in IEEE Transactions on Geoscience and Remote Sensing. This is the author's version which has not been fully edited and content may change prior to final publication. Citation information: DOI 10.1109/TGRS.2022.3174230

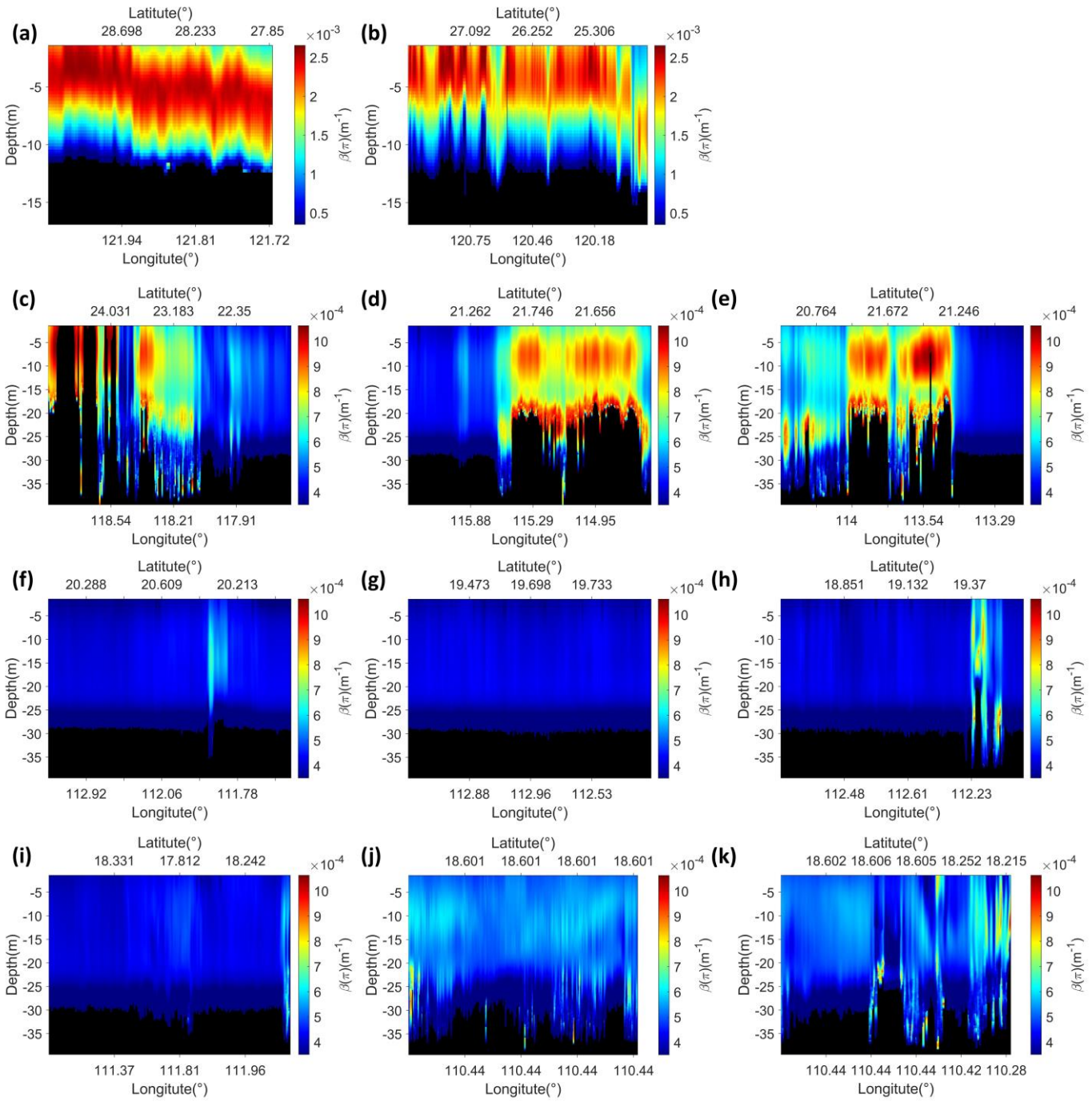

Fig. 12. Vertical distributions of the lidar-derived β(π) in seawater along the vessel traveling tracks from the ECS to the SCS. The panels ranging from (a) to (k) correspond to the lidar-estimated results from September 5 to September 15, 2020, respectively. The range values of the color bars for (a) and (b) are [0.00035 $m^{-1}sr^{-1}$: 0.0027 $m^{-1}sr^{-1}$], while it is [0.00035 $m^{-1}sr^{-1}$: 0.0011 $m^{-1}sr^{-1}$] for the color bars from (c) to (j).

This article has been accepted for publication in IEEE Transactions on Geoscience and Remote Sensing. This is the author's version which has not been fully edited and content may change prior to final publication. Citation information: DOI 10.1109/TGRS.2022.3174230

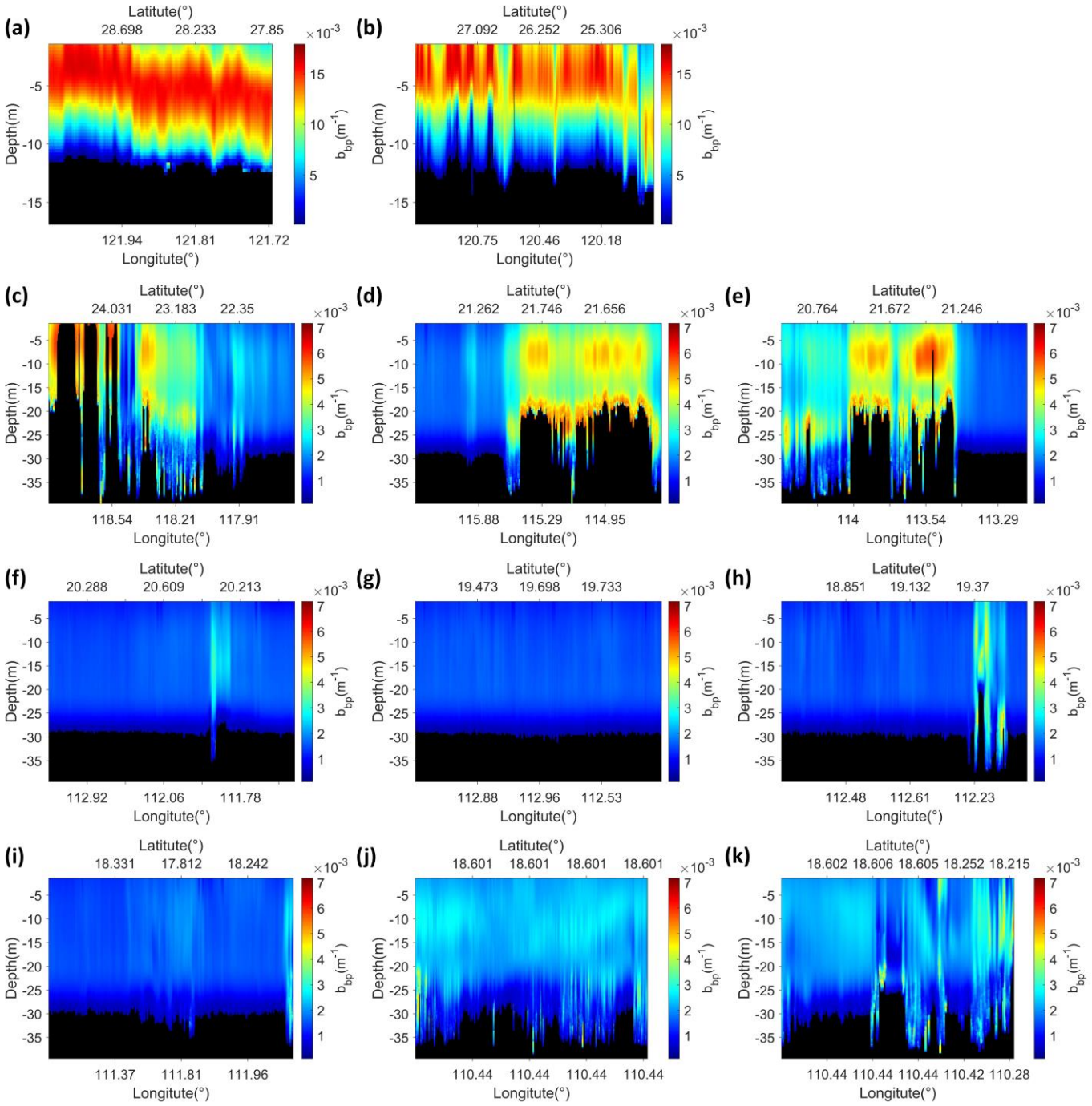

Fig. 13. Vertical distributions of the lidar-derived b_{bp} in seawater along the vessel traveling tracks from the ECS to the SCS. The panels ranging from (a) to (k) correspond to the lidar-estimated results from September 5 to September 15, 2020, respectively. The range values of the color bars for (a) and (b) are [0 m^{-1}: 0.017 m^{-1}], while it is [0 m^{-1}: 0.007 m^{-1}] for the color bars from (c) to (j).

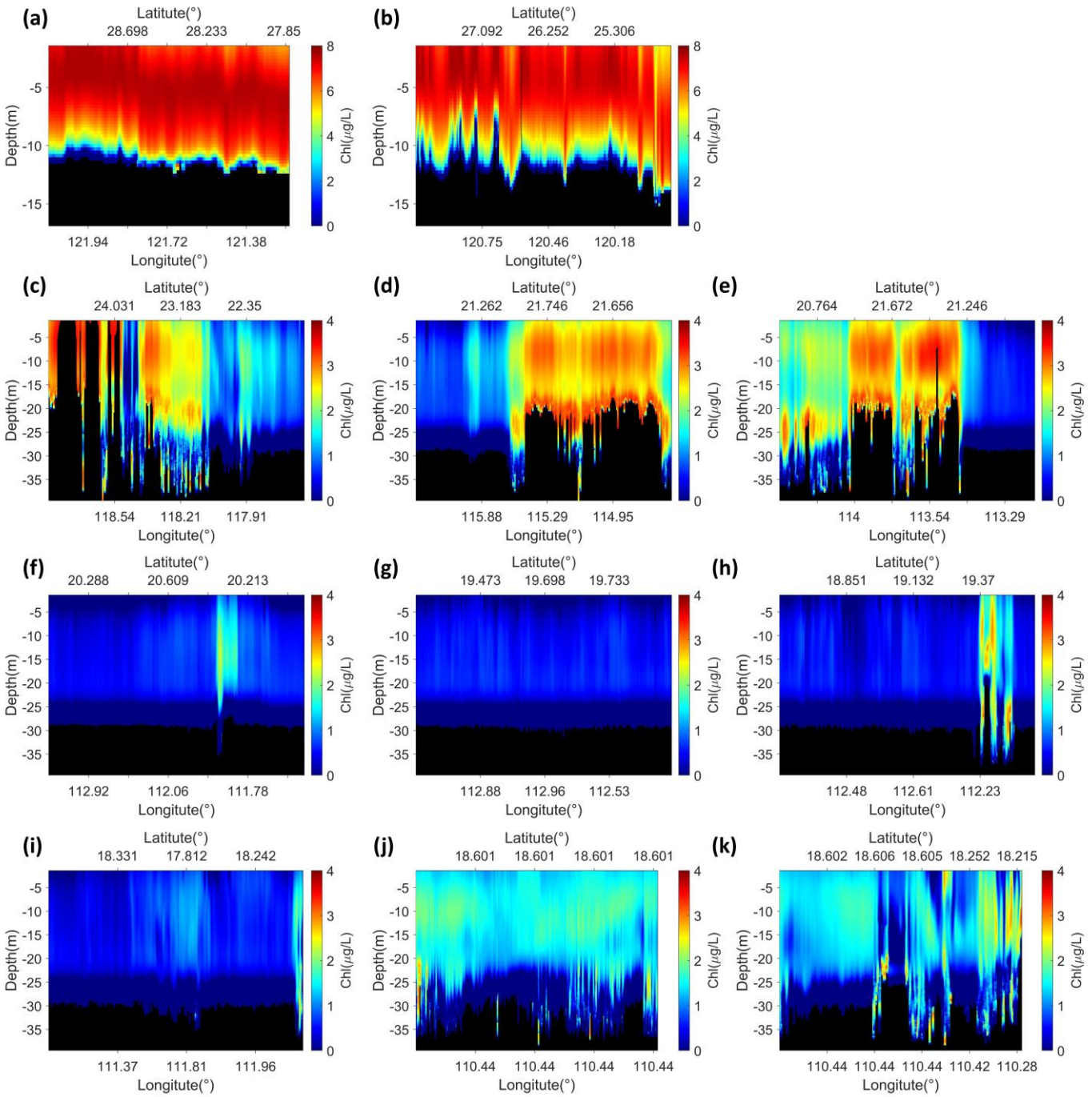

Fig. 14. Vertical distributions of lidar-derived chlorophyll-a concentration in seawater along the vessel traveling tracks from the ECS to the SCS. The panels ranging from (a) to (k) correspond to the lidar-estimated results from September 5 to September 15, 2020, respectively. The range values of the color bars for (a) and (b) are [0 μg/L: 8 μg/L], while it is [0 μg/L: 4 μg/L] for the color bars from (c) to (j).

E. Lidar-estimated vs. in situ-observed IOPs and chlorophyll-a profiles

Figure 15 shows the vertical profiles of the comparison between the lidar-estimated K_d (red dot) and in situ observed K_d (blue dot) at the stations (S21, S22, S23, S25, S28, S29, S30, S31, S32, S33, S34, S35, S36, S37, S45, S46) in the SCS obtained from September 11 to September 13. The AC-S operated unsuccessfully in very turbid seawater in the ECS and the Pearl River estuary on the other dates. Detailed in situ station information is presented in Table A1 in Appendix A. Overall, the profiles of lidar-estimated and in situ-observed values had similar levels of variability over much of the depth range, the change trend of lidar-estimated values was basically the same as the in situ-observed value, and only S25 had a lower match degree. At all stations, the K_d of the lidar-estimated value increased from 0.07 to 0.08 m^{-1} at depths of 2 to 5 m, which may be due to the backward Klett model limitation, similar results could be found in previous studies [14]. Therefore, the lidar-estimated K_d increased gradually with the signal away from the water surface. It also showed that most of the lidar-estimated value decreases after a depth of 20 m, which

may be because the signal-to-noise ratio at a certain depth after 20 m was insufficient, and the noise signal dominated after this certain depth and the signal intensity was basically not decaying too much. Therefore, the calculated K_d would then decrease gradually. The K_d of the in situ-observed value was mainly between 0.07 and 0.085 m^{-1}, and the K_d of S25 on the coast was larger and more discrete than that of the other stations, which varies from 0.08 to 0.1 m^{-1}. Figure 16 shows the vertical profiles of the comparison between the lidar-estimated b_{bp} (red dot) and in situ observed b_{bp} (blue dot) at these stations. The profiles of lidar-estimated and in situ-observed b_{bp} had similar levels of variability over much of the depth range, the change trend of lidar-estimated values was basically the same as the in situ-observed value. The b_{bp} of the in situ-observed value was mainly between 0.001 and 0.002 m^{-1}, and the b_{bp} of S25 on the coast was larger than that of the other stations, which varied from 0.0025 to 0.003 m^{-1}. There appeared subsurface scattering layers at the sites of S25 and S45 as shown in Figs. 15 and 16. In general, the lidar-estimated value was in good agreement with the in situ-measured value.

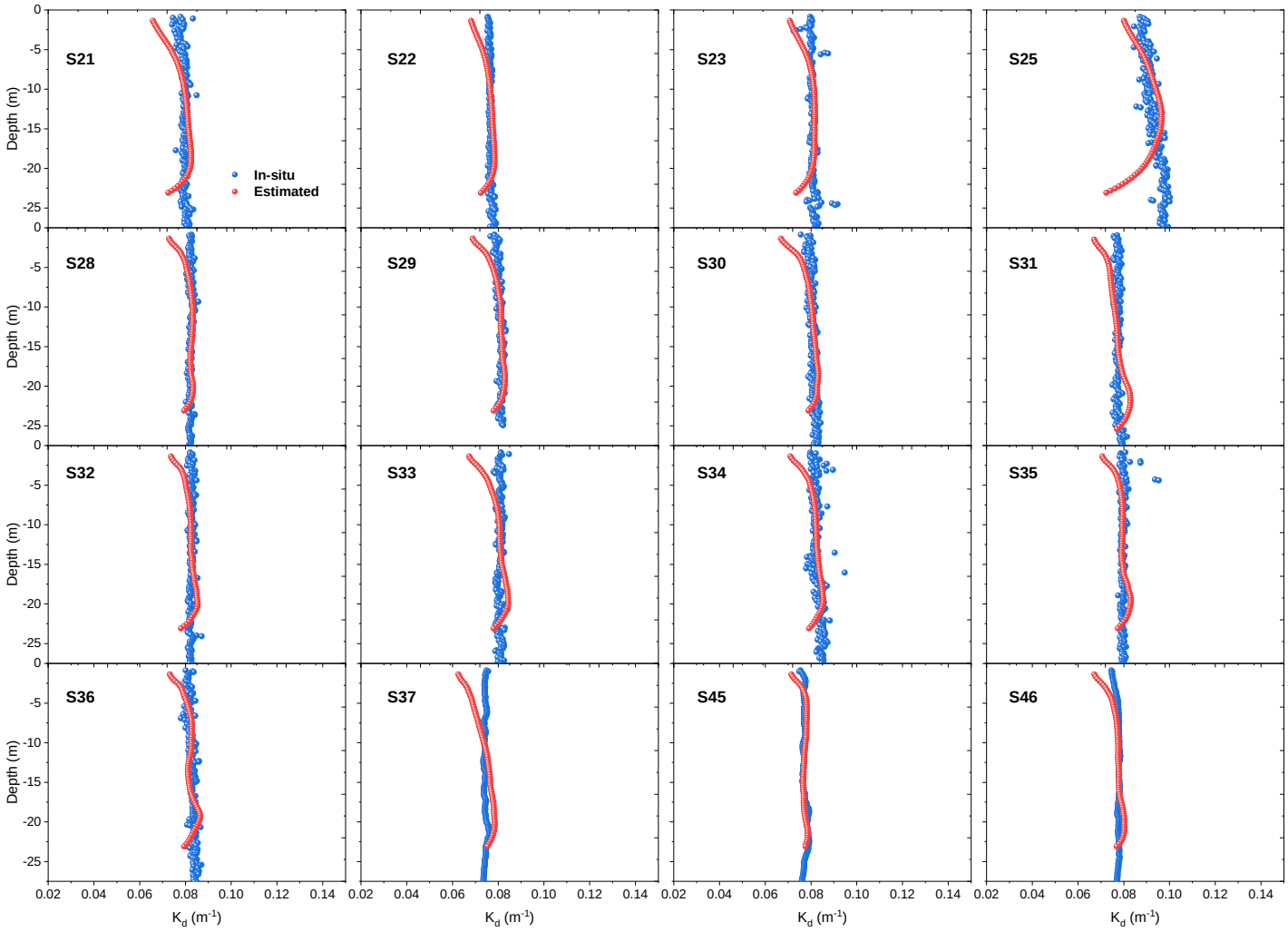

Fig. 15. Comparisons of vertical profiles between lidar-estimated and in situ-observed values at different stations. Red dots are lidar-estimated, and blue dots are in situ-observed K_d.

This article has been accepted for publication in IEEE Transactions on Geoscience and Remote Sensing. This is the author's version which has not been fully edited and content may change prior to final publication. Citation information: DOI 10.1109/TGRS.2022.3174230

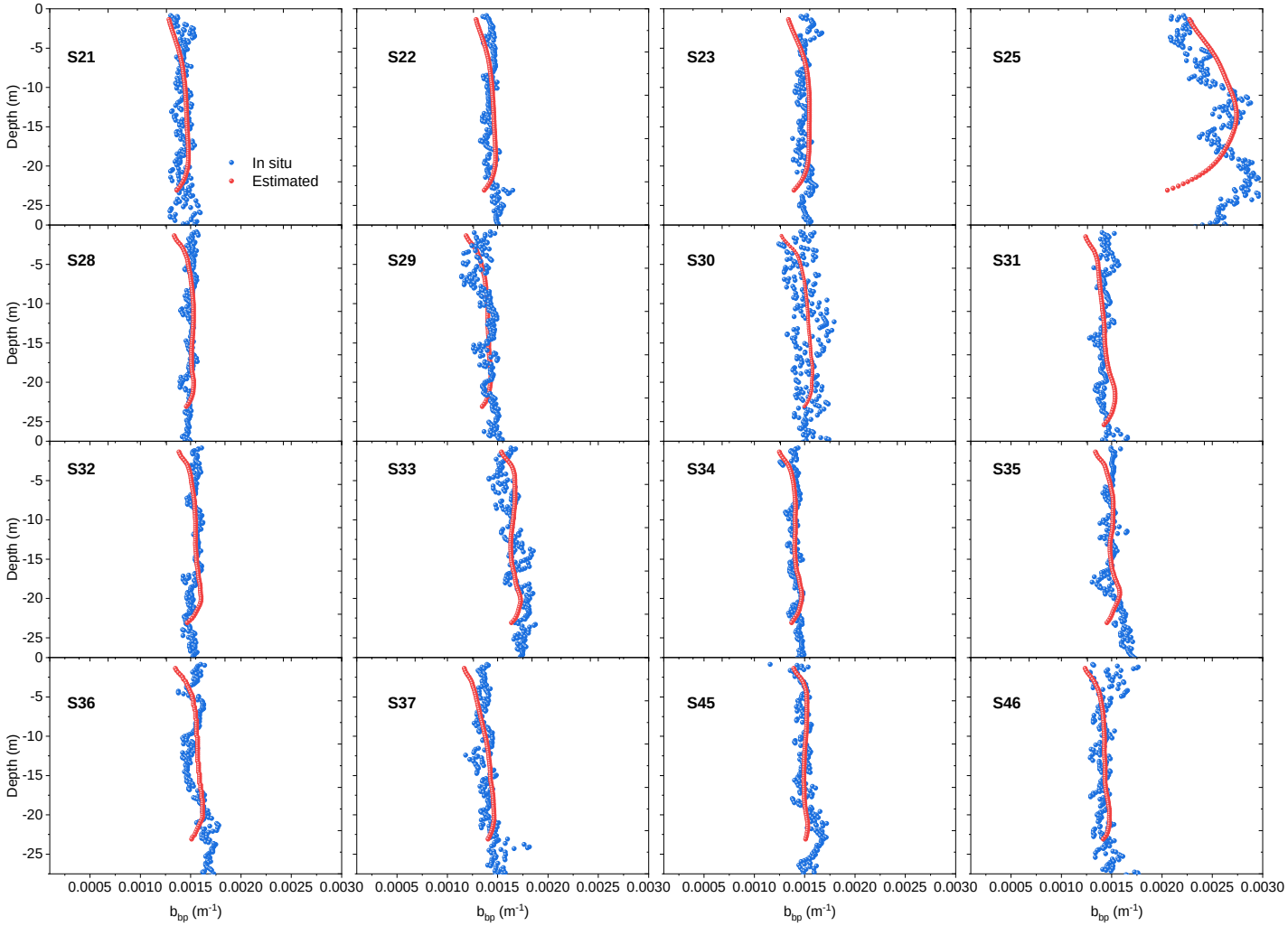

Fig. 16. Comparisons of vertical profiles between lidar-estimated and in situ-observed values at different stations. Red dots are lidar-estimated, and blue dots are in situ-observed b_{bp}.

Figure 17 shows the scatter plot of the regression analysis results between the lidar-estimated and in situ-observed K_d profiles. The correlation coefficient R^2 was 0.51, which indicated that lidar-estimated K_d was highly correlated with in situ-observed K_d, and the RMSE was 0.003 m^{-1}, which means that the dispersion of the two groups of data was small. Most of the data were between 0.07 and 0.085 m^{-1}, and only a small part of the data was between 0.09 and 0.10 m^{-1}. The normalized root mean squared error (NRMSE) [72] and mean absolute percentage error (MAPE) were also low, which were 11.5% and 29.55%, respectively. There was a slight overestimation of K_d by lidar when K_d was larger than 0.09 m^{-1}. Compared with K_d, the R^2 for the lidar-estimated and in situ-observed b_{bp} profile was higher, with value of 0.88, as shown in Figure 18 and the RMSEs was 0.0001 m^{-1}. The data were mainly concentrated between 0.0012 and 0.0018 m^{-1}. Both the NRMSE and MAPE of b_{bp} are higher than K_d, and they are 54.9% and 49.1%, respectively. There was an overestimation of b_{bp} by lidar when b_{bp} was larger than 0.0025 m^{-1}, while there is an underestimation when it was smaller than 0.0015 m^{-1}. Figure 19 shows the scatter plot of regression analysis results between lidar-estimated and in situ-observed surface chlorophyll-a concentration. Chlorophyll-a along the vertical direction were not obtained during this experiment, so the matching pairs number was much lesser than those in Figs. 17 and 18. The chlorophyll-a results show that the lidar-estimated value was highly related to the in situ-observed value, with an R^2 of 0.74, as shown in Figure 19. The RMSE for lidar-estimated chlorophyll-a data was 1.07 μg/L. Half of the data were concentrated between 0 and 1 μg/L, most of the other half were between 1 and 4 μg/L, and some data were between 5 and 8 μg/L. The NRMSE and MAPE of chlorophyll-a retrievals were the highest compared with those of K_d and b_{bp}, with values of 65.3% and 48.2%, respectively. Overall, these results showed that the proposed hybrid retrieval method was effective and robust to estimate seawater IOPs and chlorophyll-a concentration.

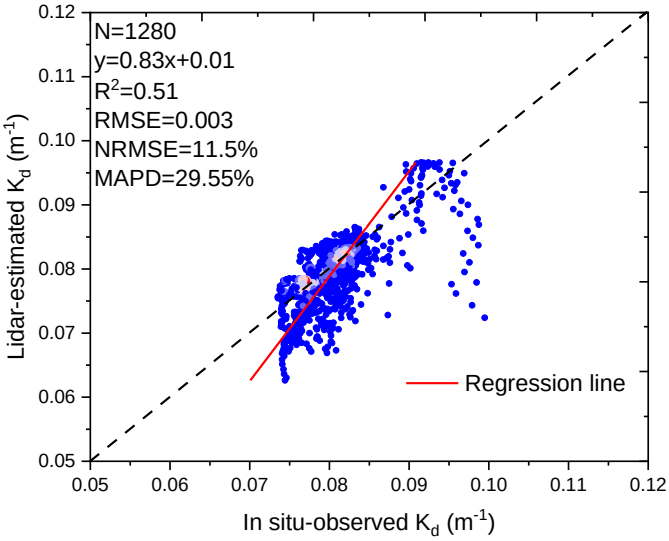

Fig. 17. Scatter plot of regression analysis results between lidar-estimated and in situ-observed K_d profiles. The points colors range from blue to red represent the points density increases.

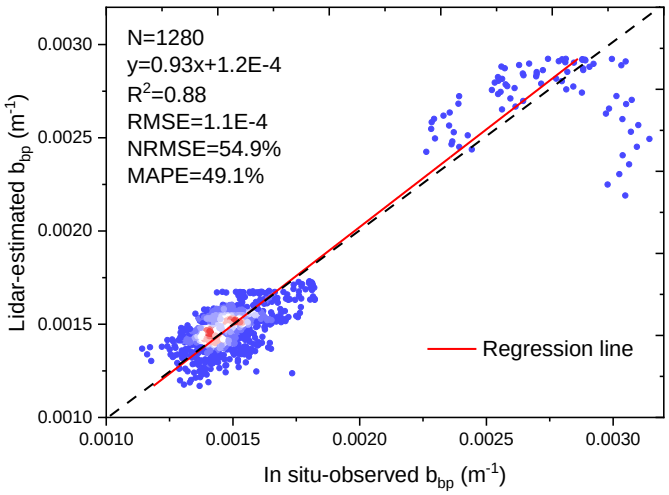

Fig. 18. Scatter plot of regression analysis results between lidar-estimated and in situ-observed b_{bp} profiles. The points colors range from blue to red represent the points density increases.

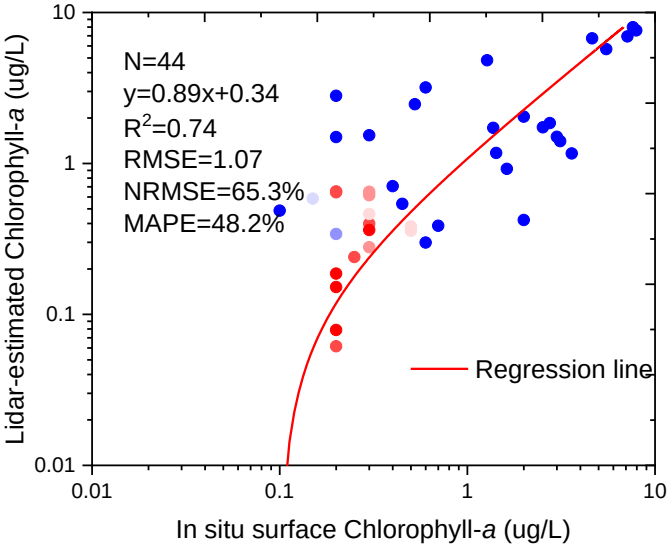

Fig. 19. Scatter plot of regression analysis results between lidar-estimated and in situ-observed surface chlorophyll-a concentration. The points colors range from blue to red represent the points density increases.

F. Lidar fluorescence and depolarization vs. in situ-observed water surface chlorophyll-a

We compared the lidar fluorescence and depolarization signals to in situ-observed water surface chlorophyll-a. Figure 20(a) shows the comparison between continuous lidar-observed fluorescence signal with discrete in situ-observed chlorophyll-a concentration. The x-axis corresponds to the entire time series of the continuous lidar measurements. During nearly two weeks of investigation, the lidar sampled more than 74,000 continuous lidar profiles. Figure 20(b) shows the regression plot for lidar fluorescence and in situ-observed chlorophyll-a concentration. We can see that there appears similar intensity change trend for lidar fluorescence signal and in situ-observed chlorophyll-a concentration as the vessel traveled in the SCS. The fluorescence signal is very noisy with a very high variability (seen samples 1-10000 in Fig. 20(a)) maybe due to the after-pulse effect on detector due to specular reflection [11, 13], because the wind was very strong during those observation times. Statistical analysis shows that the lidar fluorescence agrees well with in situ-observed chlorophyll-a concentration, with R^2 of 0.78 and RMSE of 1.04 μg/L, while the relative error is relatively high (88.5%). This may be due to that the disturbance of weak fluorescence signal by the background solar light [73]. The fluorescence efficiency variation may be another impact factor due to for the changes in functional populations of phytoplankton as the vessel traveled from the ECS to the SCS [74]. Figure 21 (a) shows the comparison between continuous lidar-observed depolarization signal with discrete in situ-observed chlorophyll-a concentration. The x-axis corresponds to the entire time series of the continuous lidar measurements. Figure 21(b) shows the regression plot for lidar depolarization and in situ-observed chlorophyll-a concentration. Statistical analysis shows that the lidar depolarization agree relatively well with in situ-observed chlorophyll-a concentration in the SCS, with the R^2 of 0.54 and the RMSE of 0.7 μg/L, while the relative error was high, with MAPE of 174.9%. No relationship was observed in the ECS coast. Compared with the correlation between lidar fluorescence and in situ-observed chlorophyll-a, the correlation decreased, and the relative error increased as well. This may be due to that the lidar fluorescence gave more reliable results than lidar depolarization due to the influence of the high load of suspended matter on the depolarization in coastal waters. Overall, our results showed that the lidar fluorescence and depolarization was feasible and effective for phytoplankton monitoring at large-scale.

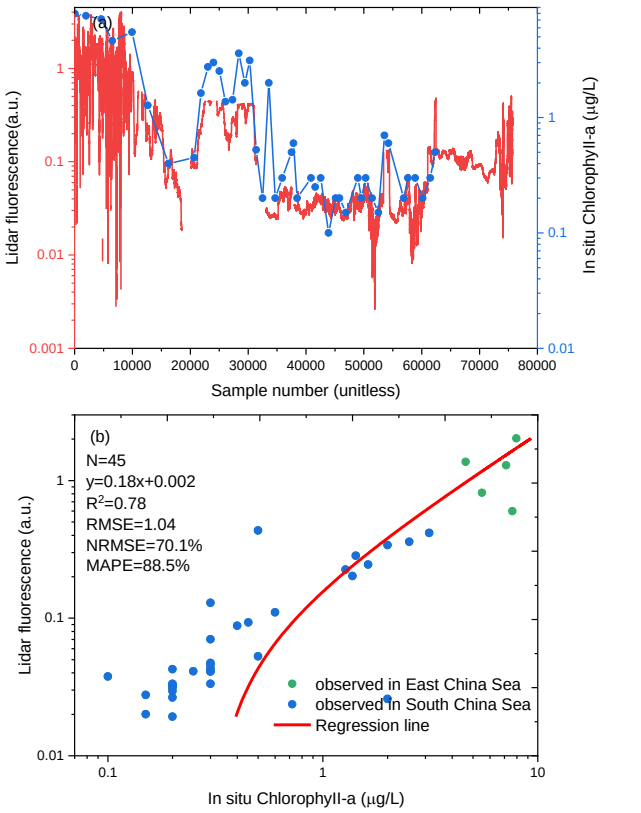

Fig. 20. Lidar fluorescence vs. in situ-observed water surface chlorophyll-a. (a) Comparison between continuous lidar-observed fluorescence signal with discrete in situ-observed chlorophyll-a; (b) Regression plot for lidar fluorescence and in situ-observed chlorophyll-a.

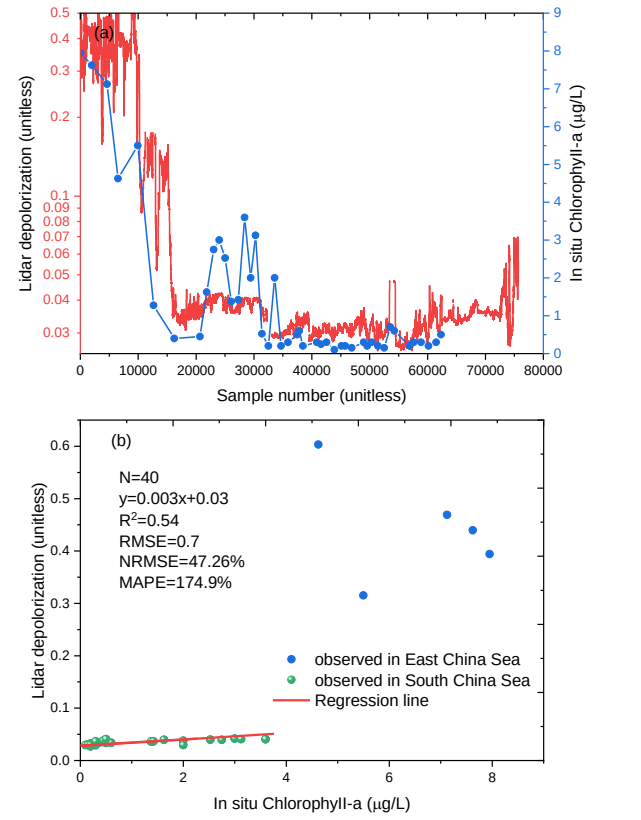

Fig. 21. Lidar depolarization vs. in situ-observed water surface chlorophyll-a. (a) Comparison between continuous lidar-observed depolarization signal with discrete in situ-observed chlorophyll-a; (b) Regression plot for lidar depolarization and in situ-observed chlorophyll-a in SCS.

G. Diurnal hourly variation in IOPs and chlorophyll-a at a fixed station

Continuous lidar measurements were collected throughout the whole day at a fixed station (110.4434°E, 18.6024°N) on the SCS coast on September 14, 2020. The fixed station was about 10 km far from the coast. Figure 22 shows the vertical distributions of IOPs and chlorophyll-a obtained by lidar at the fixed station. The panels from the top to the bottom are K_d, $\beta(\pi)$, b_{bp}, and chlorophyll-a concentration, respectively. The black masks mean the inversion failure region. The vertical distribution patterns agreed relatively well with each other. The reason is that both the factors to calculate lidar b_{bp} from lidar $\beta(\pi)$ and to calculate lidar chlorophyll-a concentration from lidar b_{bp} are constant. Accordingly, those three parameters derived from lidar definitely have exactly same trend. It also appeared that the subsurface scattering layer (SSL) occurred obviously at depths of 10 m and 20 m in the evening, with a layer thickness of approximately below 5 m, while the SSL disappeared during the daytime. The K_d of the SSL was approximately 0.14 m^{-1}, while the value in homogenous water was approximately 0.07 m^{-1}. $\beta(\pi)$ of the SSL was approximately 0.00075 $m^{-1}sr^{-1}$, while the value in homogenous water was approximately 0.00045 $m^{-1}sr^{-1}$. b_{bp} of the SSL was approximately 0.003 m^{-1}, while the value in homogenous water was approximately 0.002 m^{-1}. The chlorophyll-a concentration of the SSL was approximately 2 μg/L, which was approximately twice the value in homogenous water. Figure 23 shows hourly variations in the lidar-derived K_d, b_{bp}, and chlorophyll-a at depths of 2 m, 10 m, and 20 m during a whole day. The lidar-derived IOPs and chlorophyll-a showed similar diurnal hourly variations. The lidar-derived values at depths of 10 m and 20 m were both highest at 0:00, and they decreased gradually to their lowest values at approximately 10:00. After that time, the lidar-derived values increased gradually over time and reached their highest values at approximately 18:00. Then, they decreased gradually and reached their lowest values at approximately 22:00. Subsequently, they increased gradually over time again. These results revealed that phytoplankton varied from day to night as expected, showing the interest to use lidar technology to monitor the phytoplankton diurnal variation.

In addition, the hourly variation between tide height on the SCS coast and lidar-derived chlorophyll-a were compared during a whole day. The tide height data were obtained from the National Marine Data and Information Service (http://global-tide.nmdis.org.cn). We analyzed the day-to-night variation and high-to-low tide variation for subsurface chlorophyll-a concentration as shown in Table 2. For the day-to-night variation, we binned the data into daytime (one hour after sunrise to one hour before sunset) and nighttime (one hour after sunset to one hour before sunrise) and see if there is a statistically significant difference in the mean values of the day and night bins for each depth. For the tidal effects, we binned the data into high and low tide periods. It appeared the

subsurface chlorophyll-a concentration was a little larger at the daytime than those at the nighttime, while the mean value was higher at the ebb tide time than those at the high tide time. Figure 24 shows the plot of hourly variation comparison between tide height and lidar-estimated chlorophyll concentration at different depths. The blue, green and red lines are lidar-estimated chlorophyll at the depth of 2 m, 10 m, and 20 m, respectively, and the black line is tide height. The lidar-derived values at depths of 10 m and 20 m were both highest at 0:00, and they decreased gradually to their lowest values at approximately 8:00 for chlorophyll at the depth of 10 m, and approximately 10:00 for chlorophyll at the depth of 20 m. The amplitude of chlorophyll variation at the depth of 20 m were larger than those at the depth of 2 m and 10 m. As shown in Figures 23 and 24, the diurnal hourly variation in IOPs and chlorophyll-a was relatively lower in the early morning and midday but higher in the evening, while the relative tide height showed the reverse change trend, which revealed that the tide possibly impacted the diurnal variation in IOPs and chlorophyll-a on the SCS coast. One possible reason is that tides play an important role in the aggregation and diffusion of phytoplankton [75]. Phytoplankton may disperse with high tides because many phytoplankton may be brought into coastal waters during high tides so that the chlorophyll-a values decrease. The chlorophyll-a values increased as phytoplankton aggregated around ebb tides. The fixed station was about 10 km far from the coast hence the seawater was possibly affected by tides. The other possible reason may be due to diel vertical migration [8]. Previous studies were performed on the diel variability of IOPs in various oceanic regions [76-82]. The causes of the diel variations in optical properties remain poorly understood, including the balance between daytime production and nighttime degradation of biogenic particles (phytoplankton, bacteria, small heterotrophs), including phytoplankton excretion, cell division, and cell mortality (grazing activity and viral lyses). These biological responses depend on temperature, nutrients availability, light intensity, dynamic process and so on [80]. One note that there are relatively large uncertainties for chlorophyll-a and IOP retrievals, which may impact on the analysis of day-to-night variation. While the mean magnitude variation of chlorophyll-a concentration at the depth of 20 m between day-to-night is as large as 158% (Table 3), so the related analysis is relatively convincing. Future investigations will be carried on to reduce the retrieval uncertainty through more experiments and model study. The preliminary results indicate that the lidar remote sensing technique is feasible to monitor long-term subsurface phytoplankton structure.

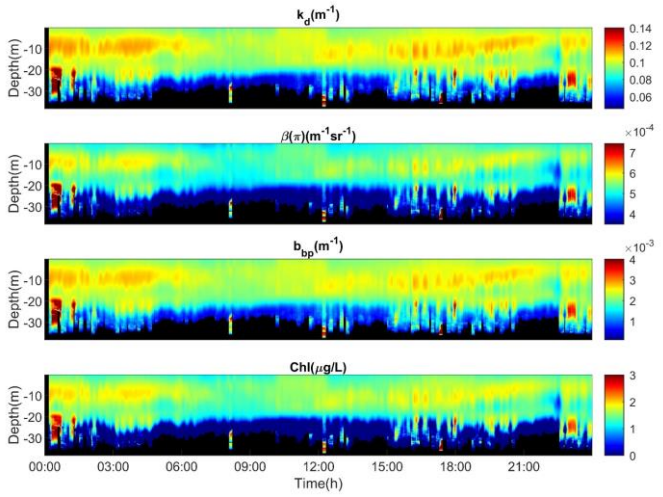

Fig. 22. Vertical distributions of IOPs and chlorophyll-a obtained by lidar throughout the whole daytime at the fixed station (110.4434°E, 18.6024°N) on September 14, 2020. The panels from the top to the bottom are K_d, β(π), b_{bp}, and chlorophyll-a, respectively.

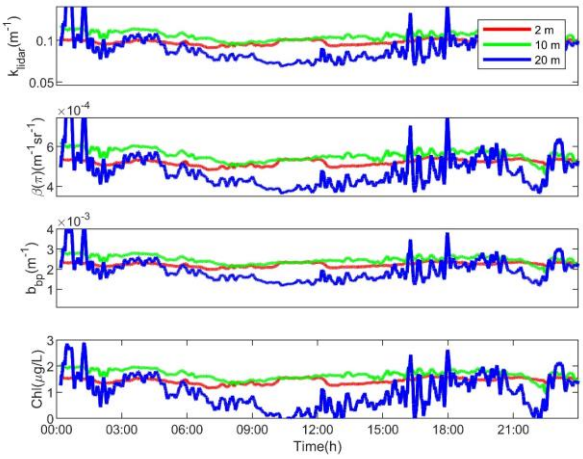

Fig. 23. Plot of the lidar-derived K_d, b_{bp}, and chlorophyll-a at depths of 2 m, 10 m and 20 m during a whole day. The panels from the top to the bottom are K_{lidar}, β(π), b_{bp}, and chlorophyll-a, respectively.

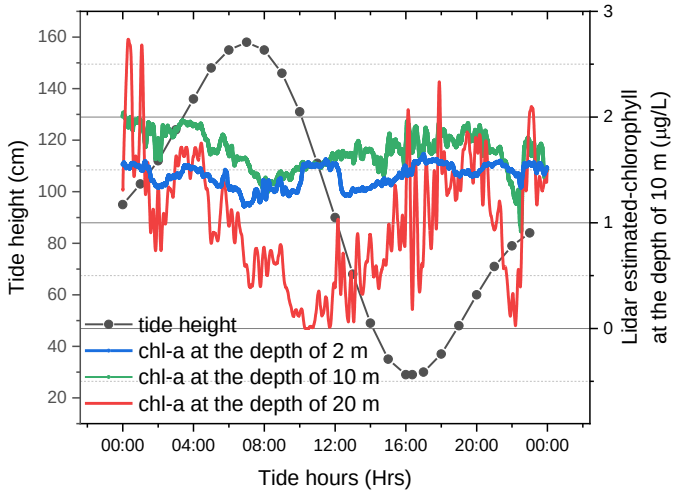

Fig. 24. Plot of hourly variation comparison between lidar-estimated chlorophyll concentration at different depths and tide height. The blue, green and red lines are lidar-estimated chlorophyll at the depth of 2 m, 10 m, and 20 m, respectively, and the black line is tide height.

TABLE 2 STATISTICAL ANALYSIS FOR DAY-TO-NIGHT VARIATION OF SUBSURFACE CHLOROPHYLL-A.

Depth of subsurface chlorophyll (m)	Mean value of the day (μg/L)	Mean value of the night (μg/L)	Mean value into high tide (μg/L)	Mean value into ebb tide (μg/L)
2	1.40	1.49	1.25	1.54
10	1.58	1.75	1.53	1.79
20	0.53	1.37	0.72	1.00

IV. SUMMARY AND CONCLUSION

In this study, spatial variations in the vertical distribution of optical properties and chlorophyll-a across two different optically-contrasted sea areas from the ECS to SCS by lidar were obtained and analyzed for the first time. During nearly two weeks of investigation, the lidar sampled more than 74,000 continuous lidar profiles, while discrete in situ measurements were obtained at 63 stations. The lidar-estimated vertical structure varied from the ECS coast to the Pearl River Estuary to the offshore and open sea of the SCS. The relative errors of lidar-estimated values for K_d , b_{bp} and chlorophyll-a concentration were 29.55%, 49.1%, and 48.2%, respectively. The above results indicate that lidar remote sensing technology was effective and feasible for different optically-contrasted ocean regions.

Statistical analysis showed that the lidar fluorescence agreed well with in situ-observed chlorophyll-a concentration, with the R^2 of 0.78, while the relative error was relatively high, with the MAPE of 88.5%. This may be due to that the weak fluorescence signal was disturbed by the background solar light. The fluorescence efficiency variation may be another impact factor due to for the changes in functional populations of phytoplankton as the vessel traveled from the ECS to the SCS. It also showed that the lidar fluorescence gave more reliable results than lidar depolarization in this experiment, which may be due to that the depolarization was influenced by the high load of suspended matter in coastal waters.

Lidar technology was used to successfully investigate the diurnal variability of IOPs and chlorophyll-a for the first time. The results showed that the diurnal hourly variation in IOPs and chlorophyll-a was relatively lower in the early morning and midday but higher in the evening, while the relative tide height showed the reverse change trend, which revealed that the tide possibly impacted the diurnal variation in IOPs and chlorophyll-a on the SCS coast. One possible reason was that tides play an important role in the aggregation and diffusion of phytoplankton. The other possible reason may be due to diel vertical migration. Overall, the above results indicate that lidar remote sensing technology is effective and feasible for day-to-night continuous monitoring. Ocean color observations cannot be provided for monitoring day-to-night changes because they are limited to sunlight. It was significant to employ the new lidar technology for phytoplankton diurnal variation monitoring.

There was a continuous, strong subsurface maximum layer at depths from approximately 2 to 5 m along the ECS coast, while the subsurface maximum layer depth dropped to approximately 10-15 m along the lidar observation track along the SCS coast. The vertical structure of the subsurface maximum layer varied over time and space. The traditional way to detect the vertical structure of optical properties and chlorophyll-a is mainly through shipboard discrete observations or Biogeochemical-Argo profiling floats, which take considerable time to cover a limited area. Compared with traditional methods, lidar has the advantages of being large-scale and long-term, and no disturbance is associated with touching measurements. It would be a good complement to passive satellite remote sensing and discrete in situ observations, which could help us to improve the estimation of phytoplankton primary productivity and carbon stocks/fluxes and to understand the temporal and spatial variation characteristics of IOPs and phytoplankton. Further investigations are needed to conduct more lidar experiments with multiple detection mechanisms for monitoring IOPs and chlorophyll-a on a larger temporal and spatial scale in the future.

APPENDIX

Supplementary data to this article can be found online at https://zenodo.org/record/6448741#.YlRgqZFBzGI.

ACKNOWLEDGMENT

We thank Zhejiang University for providing shipborne lidar data. We thank Xianliang Zhang for providing in situ measured data. We thank the National Marine Data and Information Service for providing the tide height data. We are grateful to the three anonymous reviewers for providing useful comments and criticism, which significantly improved the presentation of the paper. We also thank the editors.

REFERENCES

[1] McClain and R. Charles, "A Decade of Satellite Ocean Color Observations*," *Annual Review of Marine Science,* vol. 1, no. 1, pp. 19-42, 2009.

[2] C. Jamet *et al.*, "Going Beyond Standard Ocean Color Observations: Lidar and Polarimetry," *Frontiers in Marine Science,* vol. 6, p. 251, 2019, doi: 10.3389/fmars.2019.00251.

[3] Y. Zhuang *et al.*, "Phytoplankton Community Structure at Subsurface Chlorophyll Maxima on the Western Arctic Shelf: Patterns, Causes, and Ecological Importance," *Journal of Geophysical Research: Biogeosciences,* vol. 125, no. 6, 2020, doi: 10.1029/2019jg005570.

[4] T. Dickey, M. Lewis, and G. Chang, "Optical oceanography: Recent advances and future directions using global remote sensing and in situ observations," *Reviews of Geophysics,* vol. 44, no. 1, pp. -, 2006.

[5] H. Claustre, K. S. Johnson, and Y. Takeshita, "Observing the Global Ocean with Biogeochemical-Argo," *Annual Review of Marine Science,* vol. 12, no. 1, pp. 1-26, 2019.

[6] J. Schulien, M. J. Behrenfeld, J. W. Hair, C. Hostetler, and M. Twardowski, "Vertically- resolved phytoplankton carbon and net primary production from a high spectral resolution lidar," *optics Express,* vol. 25, pp. 13577-13587, 2017, doi: 10.1364/OE.25.013577.

[7] M. J. Behrenfeld *et al.*, "Space - based LIDAR measurements of global ocean carbon stocks," *Geophysical Research Letters,* 2013.

[8] M. Behrenfeld *et al.*, "Global satellite-observed daily vertical migrations of ocean animals," *Nature,* vol. 576, 12/01 2019, doi: 10.1038/s41586-019-1796-9.

[9] J. H. Churnside, R. D. Marchbanks, S. Vagle, S. W. Bell, and P. J. Stabeno, "Stratification, plankton layers, and mixing measured by airborne lidar in the Chukchi and Beaufort seas," *Deep Sea Research Part II Topical Studies in Oceanography*, p. 104742, 2020.

[10] J. H. Churnside and P. L. Donaghay, "Thin scattering layers observed by airborne lidar," *ICES Journal of Marine Science: Journal du Conseil*, vol. 66(4), pp. 778-789, 2009.

[11] X. Lu, Y. Hu, Y. Yang, P. Bontempi, A. Omar, and R. Baize, "Antarctic spring ice-edge blooms observed from space by ICESat-2," *Remote Sensing of Environment*, p. 111827, 05/01 2020, doi: 10.1016/j.rse.2020.111827.

[12] C. A. Hostetler, M. J. Behrenfeld, Y. Hu, J. W. Hair, and J. A. Schulien, "Spaceborne Lidar in the Study of Marine Systems," *Annual Review of Marine Science*, vol. 10, no. 1, pp. 121-147, 2018/01/03 2018, doi: 10.1146/annurev-marine-121916-063335.

[13] X. Lu, Y. Hu, C. Trepte, S. Zeng, and J. H. Churnside, "Ocean subsurface studies with the CALIPSO spaceborne lidar," *Journal of Geophysical Research: Oceans*, vol. 119, no. 7, pp. 4305-4317, 2014.

[14] H. Liu, P. Chen, Z. Mao, and D. Pan, "Iterative retrieval method for ocean attenuation profiles measured by airborne lidar," *Applied Optics*, vol. 59, no. 10, pp. C42-C51, 2020/04/01 2020, doi: 10.1364/AO.379406.

[15] P. Chen and D. Pan, "Ocean Optical Profiling in South China Sea Using Airborne LiDAR," *Remote Sensing*, vol. 11, no. 15, p. 1826, 2019. [Online]. Available: https://www.mdpi.com/2072-4292/11/15/1826.

[16] B. L. Collister, R. C. Zimmerman, C. I. Sukenik, V. J. Hill, and W. M. Balch, "Remote sensing of optical characteristics and particle distributions of the upper ocean using shipboard lidar," *Remote Sensing of Environment*, vol. 215, pp. 85-96, 2018.

[17] J. H. Churnside and R. D. Marchbanks, "Inversion of oceanographic profiling lidars by a perturbation to a linear regression," *Applied Optics*, vol. 56, no. 18, pp. 5228-5233, 2017.

[18] J. H. Lee, J. H. Churnside, R. D. Marchbanks, P. L. Donaghay, and J. M. Sullivan, "Oceanographic lidar profiles compared with estimates from in situ optical measurements," *Applied Optics*, vol. 52, no. 4, pp. 786-794, 2013/02/01 2013, doi: 10.1364/AO.52.000786.

[19] Y. Ma, N. Xu, Z. Liu, B. Yang, and S. Li, "Satellite-derived bathymetry using the ICESat-2 lidar and Sentinel-2 imagery datasets," *Remote Sensing of Environment*, vol. 250, p. 112047, 2020.

[20] C. E. Parrish, L. A. Magruder, A. L. Neuenschwander, N. Forfinski-Sarkozi, M. Alonzo, and M. Jasinski, "Validation of ICESat-2 ATLAS Bathymetry and Analysis of ATLAS's Bathymetric Mapping Performance," *Remote Sensing*, vol. 11, no. 14, p. 1634, 2019. [Online]. Available: https://www.mdpi.com/2072-4292/11/14/1634.

[21] M. R. Roddewig *et al.*, "Airborne lidar detection and mapping of invasive lake trout in Yellowstone Lake," *Appl Opt*, vol. 57, p. 4111, 2018, doi: 10.1364/AO.57.004111.

[22] M. R. Roddewig, N. J. Pust, J. H. Churnside, and J. A. Shaw, "Dual-polarization airborne lidar for freshwater fisheries management and research," *Optical Engineering*, vol. 56, no. 3, p. 031221, 2017.

[23] J. Churnside, D. Demer, and B. Mahmoudi, *A comparison of lidar and echosounder measurements of fish schools in the Gulf of Mexico*. 2003, pp. 147-154.

[24] J. H. Churnside, A. F. Sharov, and R. A. Richter, "Aerial surveys of fish in estuaries: a case study in Chesapeake Bay," *Ices Journal of Marine Science*, vol. 68, no. 1, pp. 239-244, 2011.

[25] J. H. Churnside, J. J. Wilson, and V. V. Tatarskii, "Lidar profiles of fish schools," *Applied Optics*, vol. 36, no. 24, pp. 6011-20, 1997.

[26] P. Chen *et al.*, "Vertical distribution of subsurface phytoplankton layer in South China Sea using airborne lidar," *Remote Sensing of Environment*, vol. 263, p. 112567, 2021/09/15/ 2021, doi: https://doi.org/10.1016/j.rse.2021.112567.

[27] P. Chen, Z. Mao, Z. Zhang, H. Liu, and D. Pan, "Detecting subsurface phytoplankton layer in Qiandao Lake using shipborne lidar," *Optics Express*, vol. 28, no. 1, pp. 558-569, 2020/01/06 2020, doi: 10.1364/OE.381617.

[28] T. S. Moore *et al.*, "Vertical distributions of blooming cyanobacteria populations in a freshwater lake from LIDAR observations," *Remote Sensing of Environment*, vol. 225, pp. 347-367, 2019.

[29] H. Liu, P. Chen, Z. Mao, D. Pan, and Y. He, "Subsurface plankton layers observed from airborne lidar in Sanya Bay, South China Sea," *Optics Express*, vol. 26, no. 22, pp. 29134-29147, 2018/10/29 2018, doi: 10.1364/OE.26.029134.

[30] J. H. Churnside and R. D. Marchbanks, "Subsurface plankton layers in the Arctic Ocean," *Geophysical Research Letters*, vol. 42, no. 12, pp. 4896-4902, 2015.

[31] J. Churnside, R. D. Marchbanks, J. H. Lee, J. Shaw, A. Weidemann, and P. L. Donaghay, *Airborne lidar detection and characterization of internal waves in a shallow Fjord*. 2012, p. 3611.

[32] J. Churnside, "Lidar signature from bubbles in the sea," *Optics Express*, vol. 18, pp. 8294-9, 2010, doi: 10.1364/OE.18.008294.

[33] P. Chen, D. Pan, Z. Mao, and H. Liu, "A Feasible Calibration Method for Type 1 Open Ocean Water LiDAR Data Based on Bio-Optical Models," *Remote Sensing*, vol. 11, no. 2, p. 172, 2019. [Online]. Available: http://www.mdpi.com/2072-4292/11/2/172.

[34] Z. P. Lee, M. Darecki, K. L. Carder, C. O. Davis, D. Stramski, and W. J. Rhea, "Diffuse attenuation coefficient of downwelling irradiance: An evaluation of remote sensing methods," *Journal of Geophysical Research Oceans*, vol. 110, no. C2, 2005.

[35] C. Amante and B. W. Eakins, "ETOPO1 1 Arc-Minute Global Relief Model: Procedures, Data Sources and Analysis," *Psychologist*, vol. 16, no. 3, pp. 20 - 25, 2009.

[36] J. D. Klett, "Stable analytical inversion solution for processing lidar returns," *Applied optics*, vol. 20, no. 2, pp. 211-220, 1981.

[37] P. Chen, C. Jamet, Z. Mao, and D. Pan, "OLE: A Novel Oceanic Lidar Emulator," *IEEE Transactions on Geoscience and Remote Sensing*, vol. 59, no. 11, pp. 9730-9744, 2021, doi: 10.1109/TGRS.2020.3035381.

[38] P. Chen, D. Pan, Z. Mao, and H. Liu, "Semi-analytic Monte Carlo radiative transfer model of laser propagation in inhomogeneous sea water within subsurface plankton layer," *Optics & Laser Technology*, vol. 111, pp. 1-5, 2019/04/01/ 2019, doi: https://doi.org/10.1016/j.optlastec.2018.09.028.

[39] J. H. Churnside, "Review of profiling oceanographic lidar," *Optical Engineering*, vol. 53, no. 5, pp. 051405-051405, 2014.

[40] H. R. Gordon, "Interpretation of airborne oceanic lidar: effects of multiple scattering," *Applied Optics*, vol. 21, no. 16, pp. 2996-3001, 1982.

[41] L. Hu, X. Zhang, Y. Xiong, D. J. Gray, and M. X. He, "Variability of relationship between the volume scattering function at 180° and the backscattering coefficient for aquatic particles," *Applied Optics*, vol. 59, no. 10, 2020.

[42] J. F. Berthon, E. Shybanov, E. G. Lee, and G. Zibordi, "Measurements and modeling of the volume scattering function in the coastal northern Adriatic Sea," *Applied Optics*, vol. 46, no. 22, pp. 5189-203, 2007.

[43] X. Zhang, D. J. Gray, Y. Huot, Y. You, and L. Bi, "Comparison of optically derived particle size distributions: scattering over the full angular range versus diffraction at near forward angles," *Applied Optics*, vol. 51, no. 21, p. 5085, 2012.

[44] J. M. Sullivan and M. S. Twardowski, "Angular shape of the oceanic particulate volume scattering function in the backward direction," *Applied Optics*, vol. 48, no. 35, pp. 6811-9, 2009.

[45] M. Chami, A. Thirouard, and T. Harmel, "POLVSM (Polarized Volume Scattering Meter) instrument: an innovative device to measure the directional and polarized scattering properties of hydrosols," *Optics Express*, vol. 22, no. 21, pp. 26403-28, 2014.

[46] J. M. Sullivan and M. S. J. A. O. Twardowski, "Angular shape of the oceanic particulate volume scattering function in the backward direction," vol. 48, no. 35, pp. 6811-6819, 2009.

[47] X. Zhang, E. Boss, and D. J. J. O. e. Gray, "Significance of scattering by oceanic particles at angles around 120 degree," vol. 22, no. 25, pp. 31329-31336, 2014.

[48] J. H. Churnside, J. M. Sullivan, and M. S. Twardowski, "Lidar extinction-to-backscatter ratio of the ocean," *Optics express*, vol. 22, no. 15, pp. 18698-18706, 2014.

[49] M. Chami, E. Marken, J. Stamnes, G. Khomenko, and G. J. J. o. G. R. O. Korotaev, "Variability of the relationship between the particulate backscattering coefficient and the volume scattering function measured at fixed angles," vol. 111, no. C5, 2006.

[50] E. Boss and W. S. J. A. O. Pegau, "Relationship of light scattering at an angle in the backward direction to the backscattering coefficient," vol. 40, no. 30, pp. 5503-5507, 2001.

[51] A. L. Whitmire, W. S. Pegau, L. Karp-Boss, E. Boss, and T. J. J. O. E. Cowles, "Spectral backscattering properties of marine phytoplankton cultures," vol. 18, no. 14, pp. 15073-15093, 2010.

[52] R. A. Maffione and D. R. Dana, "Instruments and methods for measuring the backward-scattering coefficient of ocean waters," *Applied Optics*, vol. 36, no. 24, pp. 6057-67, 1997.

[53] J. M. Sullivan, M. S. Twardowski, J. Zaneveld, and C. Moore, *Measuring optical backscattering in water*. Springer Berlin Heidelberg, 2013.

[54] M. Kheireddine, R. J. W. Brewin, M. Ouhssain, and B. J. Jones, "Particulate scattering and backscattering in relation to the nature of particles in the Red Sea," *Journal of Geophysical Research Oceans*, 2021.

[55] Y. I. Kopilevich, M. E. Kononenko, and E. I. J. J. j. P. Zadorozhnaya, "The effect of the forward-scattering index on the characteristics of a light beam in sea water," vol. 77, no. 10, pp. 598-0, 2010.

[56] Y. I. Kopilevich and A. G. Surkov, "Mathematical modeling of the input signals of oceanological lidars," *Journal of Optical Technology C/c of Opticheskii Zhurnal*, vol. 75, no. 5, pp. 321-326, 2008.

[57] R. E. Walker and J. W. McLean, "Lidar equations for turbid media with pulse stretching," *Applied Optics*, vol. 38, no. 12, pp. 2384-2397, 1999.

[58] J. W. Mclean, J. D. Freeman, and R. E. Walker, "Beam spread function with time dispersion," *Applied Optics*, vol. 37, no. 21, p. 4701, 1998.

[59] D. Dionisi, V.E., Brando, G., Volpe, S., Colella and R. Santoleri, "Seasonal distributions of ocean particulate optical properties from spaceborne lidar measurements in Mediterranean and Black Sea," *Remote Sensing of Environment*, vol. 247, 2020, doi: 10.1016/j.rse.2020.111889.

[60] J. C. Ramella-Roman, S. A. Prahl, and S. L. Jacques, "Three Monte Carlo programs of polarized light transport into scattering media: part I," *Optics Express*, vol. 13, no. 12, pp. 4420-4438, 2005.

[61] M. R. Roddewig, J. H. Churnside, and J. A. Shaw, "Airborne lidar detection of an underwater thermal vent," *Journal of Applied Remote Sensing*, vol. 11, no. 3, p. 036014, 2017.

[62] J. H. Churnside, "Polarization effects on oceanographic lidar," *Optics Express*, vol. 16, no. 2, pp. 1196-207, 2008.

[63] J. Luo *et al.*, "Rotating a half-wave plate by 45°: An ideal calibration method for the gain ratio in polarization lidars," *Optics Communications*, vol. 407, pp. 361-366, 2018.

[64] P. Chen, D. Pan, T. Wang, Z. Mao, and Y. Zhang, "Coastal and inland water monitoring using a portable hyperspectral laser fluorometer," *Marine Pollution Bulletin*, vol. 119, no. 1, pp. 153-161, 6/15/ 2017, doi: https://doi.org/10.1016/j.marpolbul.2017.03.057.

[65] P. Chen, D. Pan, Z. Mao, and B. Tao, "Detection of water quality parameters in Hangzhou Bay using a portable laser fluorometer," *Marine Pollution Bulletin*, vol. 93, no. 1–2, pp. 163-171, 4/15/ 2015, doi: http://dx.doi.org/10.1016/j.marpolbul.2015.01.023.

[66] A. Morel, "Optical properties of pure water and pure sea water," *Optical aspects of oceanography*, vol. 1, no. 1, pp. 1-24, 1974.

[67] A. Morel and S. Maritorena, "Bio-optical properties of oceanic waters: A reappraisal," *JOURNAL OF GEOPHYSICAL RESEARCH*, 2001.

[68] J. W. Robert *et al.*, "Particle backscattering as a function of chlorophyll and phytoplankton size structure in the open-ocean," *Optics express*, 2012.

[69] M. Bellacicco *et al.*, "Global Variability of Optical Backscattering by Non ` lgal particles From a Biogeochemical || rgo Data Set," *Geophysical Research Letters*, vol. 46, 2019.

[70] Y. Huot, A. Morel, M. S. Twardowski, D. Stramski, and R. A. Reynolds, "Particle optical backscattering along a chlorophyll gradient in the upper layer of the eastern South Pacific Ocean," *Biogeosciences,5,2(2008-04-07)*, vol. 5, no. 2, pp. 495-507, 2008.

[71] H. R. Gordon and A. Y. Morel, "Remote Assessment of Ocean Color for Interpretation of Satellite Visible Imagery," *Springer US*, 1983.

[72] G. Piñeiro, S. Perelman, J. P. Guerschman, and J. M. Paruelo, "How to evaluate models: Observed vs. predicted or predicted vs. observed?," *Ecological Modelling*, vol. 216, no. 3, pp. 316-322, 2008/09/10/ 2008, doi: https://doi.org/10.1016/j.ecolmodel.2008.05.006.

[73] D. Thoren, P. Thoren, and U. Schmidhalter, "Influence of ambient light and temperature on laser-induced chlorophyll fluorescence measurements," *European Journal of Agronomy - EUR J AGRON*, vol. 32, pp. 169-176, 02/01 2010, doi: 10.1016/j.eja.2009.10.003.

[74] S. A. Mosharov, V. M. Sergeeva, V. V. Kremenetskiy, A. F. Sazhin, and S. V. Stepanova, "Assessment of phytoplankton photosynthetic efficiency based on measurement of fluorescence parameters and radiocarbon uptake in the Kara Sea," *Estuarine, Coastal and Shelf Science*, vol. 218, pp. 59-69, 2019/03/05/ 2019, doi: https://doi.org/10.1016/j.ecss.2018.12.004.

[75] J. Chen, W. Ye, J. Guo, Z. Luo, and Y. Li, "Diurnal Variability in Chlorophyll-a, Carotenoids, CDOM and SO_4(2-) Intensity of Offshore Seawater Detected by an Underwater Fluorescence-Raman Spectral System," *Sensors (Basel)*, vol. 16, no. 7, doi: 10.3390/s16071082.

[76] D. A. Siegel, T. D. Dickey, L. Washburn, M. K. Hamilton, and B. G. Mitchell, "Optical determination of particulate abundance and production variations in the oligotrophic ocean," *Deep Sea Research Part A Oceanographic Research Papers*, vol. 36, no. 2, pp. 211-222, 1989.

[77] H. Claustre, A. Morel, M. Babin, C. Cailliau, and D. Vaulot, "Variability in particle attenuation and chlorophyll fluorescence in the Tropical Pacific: Scales, patterns, and biogeochemical implications," *Journal of Geophysical Research Atmospheres*, vol. 104, no. C2, pp. 3401-3422, 1999.

[78] P. Gernez, D. Antoine, and Y. Huot, "Diel cycles of the particulate beam attenuation coefficient under varying trophic conditions in the northwestern Mediterranean Sea: Observations and modeling," *Limnology & Oceanography*, vol. 56, no. 1, 2011.

[79] Daniel, Vaulot, Dominique, and Marie, "Diel variability of photosynthetic picoplankton in the equatorial Pacific," *Journal of Geophysical Research: Oceans*, 1999.

[80] M. Kheireddine and D. Antoine, "Diel variability of the beam attenuation and backscattering coefficients in the northwestern Mediterranean Sea (BOUSSOLE site)," *Journal of Geophysical Research Oceans*, vol. 119, no. 8, pp. 5465-5482, 2015.

[81] T.-Y. Chen, C.-C. Lai, J.-H. Tai, C.-Y. Ko, and F.-K. Shiah, "Diel to Seasonal Variation of Picoplankton in the Tropical South China Sea," (in English), *Frontiers in Marine Science*, Original Research vol. 8, no. 1460, p. 732017, 2021-October-21 2021, doi: 10.3389/fmars.2021.732017.

[82] F. Henderikx Freitas *et al.*, "Diel variability of bulk optical properties associated with the growth and division of small phytoplankton in the North Pacific Subtropical Gyre," (in eng), *Appl Opt*, vol. 59, no. 22, pp. 6702-6716, Aug 1 2020, doi: 10.1364/ao.394123.

Peng Chen received the B.S., M.S., and Ph.D. degrees in Wuhan University. Now he works in the State Key Laboratory of Satellite Ocean Environment Dynamics, Second Institute of Oceanography, Ministry of Natural Resources. His work broadly concentrates on lidar remote sensing of ocean ecological environment. He conducts research on ocean lidar signal simulation for guiding lidar sensor design and understanding the interaction between laser and various substances in seawater. Besides, he develops a range of inversion methods from lidar echo signals, to obtain the vertical structure of ocean ecological environment. Based on the lidar remote sensing products, he analyzes the spatial and diurnal variation in the vertical distribution of phytoplankton and interprets its dynamic process and driving mechanism.